

Universiteit
Leiden
The Netherlands

Glycosyl cations in glycosylation reactions

Hansen, T.

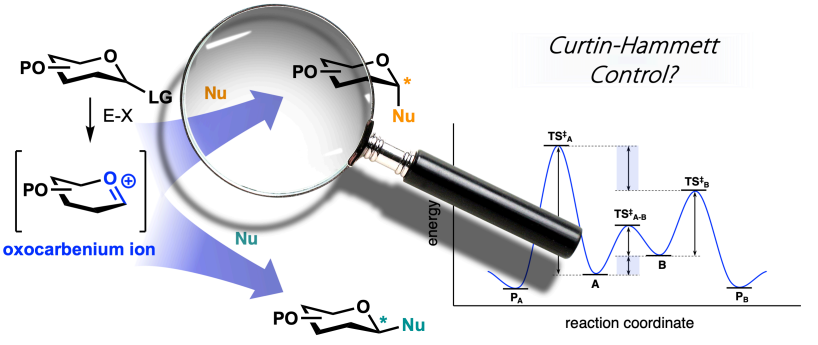
Citation
Hansen, T. (2020, November 25). *Glycosyl cations in glycosylation reactions*. Retrieved from https://hdl.handle.net/1887/138249

Version:	Publisher's Version
License:	Licence agreement concerning inclusion of doctoral thesis in the Institutional Repository of the University of Leiden
Downloaded from:	https://hdl.handle.net/1887/138249

Note: To cite this publication please use the final published version (if applicable).

Chapter 3

Dissecting Curtin-Hammett Scenarios for Addition Reactions to Glycosyl Oxocarbenium Ions



Abstract | Glycosyl cations play an all-important role in glycosylation reactions, determining the reactivity of glycosylating agents and shaping the stereoselectivity. Notwithstanding the high reactivity of these species, they can be at the basis of highly stereoselective addition reactions. The nature of the incoming nucleophile also plays an important role, and it has been difficult to delineate clear structure-reactivity-stereoselectivity relationships for addition reactions to glycosyl oxocarbenium ions, hampering the development of stereoselective glycosylation methodologies. We show in this chapter how the nature of typical S_N1-nucleophiles, *i.e.*, triethyl deuteriosilane (TES-*d*) and allyltrimethylsilane (allyl-TMS) affects the stereochemical outcome of addition reactions to glycosyl cations. TES-*d* adds to oxocarbenium ions following a barrierless reaction pathway, and the stereoselectivity of these reactions can be reliably predicted and understood from the distribution of the cation conformers, the stability of which is dictated by the nature and orientation of the ring substituents. The stereoselectivity of the addition reactions of allyl-TMS, however, often does not mirror the mixture of glycosyl cation conformers. For these reactions we have computationally dissected Curtin-Hammett kinetic scenarios to accurately show how the outcome of these addition reactions is influenced by the reactivity of the different glycosyl oxocarbenium ion conformers and the incoming nucleophile. By performing activation strain and Kohn-Sham molecular orbital analyses, it was found that the disparate stereoselectivity originates from (i) the stability of the different glycosyl cation conformers; (ii) the position of the transition state along the reaction coordinate; and (iii) the (steric) Pauli repulsion between the nucleophile and the glycosyl cation. The offered quantitative mechanistic insights will serve as a guide for the interpretation of glycosylation results and as the basis to further explore addition reaction mechanisms to cyclic carbocations.

Introduction

Six-membered oxocarbenium ions are important reactive intermediates in organic synthesis. The stability of glycosyl oxocarbenium ions determines the reactivity of glycosyl donors and plays a paramount role in the stereochemical outcome of glycosylation reactions.[1–13] The intrinsic high reactivity and fleeting nature of glycosyl oxocarbenium ions represents a major challenge in studying these species and determining clear structure−reactivity-stereoselectivity principles. Due to the extremely short lifetime of these intermediates,[14,15] there is currently no (spectroscopic) technique available in conventional reaction media to study these species in a direct manner and assess their behavior, leaving a major gap in our understanding of reactions involving these ions.[16–24] Therefore, computational techniques have been used to gain insight into their structure and reactivity.

Chapter 2 reported on a strategy to map the complete conformational space an oxocarbenium ion can adopt to establish the conformational preference of these species. The shape of the cations, preferentially adopting flattened structures to allow stabilization of the cationic sp^2-hybridized carbon by delocalization of electron density from the adjacent oxygen, is influenced by the substituents on the ring.[18,25–28] Electron-rich substituents (*e.g.*, *O*-, *N*-, *F*-moieties) at the C3- and C4-position prefer to adopt an axial position, while at the C2-position these groups have a preference for a *pseudo*-equatorial position. Various experimental studies have shown that the conformation of a glycosyl cation can have a significant impact on the stereoselectivity of reactions, in which these ions can form.[1,16,18,29–32] In Chapter 2 it was shown that oxocarbenium ions can be trapped using triethylsilane-*d* (TES-*d*) to reveal the conformational preference of the cations. Highly stereoselective addition reactions were observed for oxocarbenium ions, that preferentially take up a single structure (or family of closely related structures). Diastereomeric mixtures were obtained when oxocarbenium ions were formed that could adopt different low energy conformations. Notably, some addition reactions described in Chapter 2, proceeded with a markedly different stereochemical outcome than analogous reactions reported in literature using different typical S_N1-nucleophiles. As shown in Figure 1A, the addition of TES-*d* to a mannosyl oxocarbenium ion, that preferentially adopts a $^3H_4$-half chair conformation, takes place from the top side of the cation to provide the β-linked product with excellent diastereoselectivity (97:3). In contrast, the addition of allyl-trimethylsilane (allyl-TMS) provides a mixture of anomers (34:66), in which the opposite anomer (*i.e.*, the α-linked product) prevails.[18,33]

The difference in stereochemical outcome may be explained by invoking different kinetic scenarios for the addition of the nucleophile to the oxocarbenium ion conformers. Figure 1B-D shows three relevant Curtin-Hammett scenarios[34,35] for the addition of a nucleophile to an oxocarbenium ion, that can adopt two relatively stable conformers **A** and

B. These scenarios can be divided into two classes: in the first class (class I, Figure 1B), the barrier for interconversion of the oxocarbenium ion conformers **A** and **B** is higher than the barrier of the addition reactions to both, while in the second class (class II-a and II-b, Figure 1C-D) the barrier for the addition is higher than the barrier for interconversion. For class I, the outcome is determined by the difference in energy between oxocarbenium ion conformers **A** and **B** ($\Delta\Delta G°$). While for class II the difference in activation energies of the transition states (TSs, $\Delta\Delta G^{‡}$) leading from the oxocarbenium ions conformers **A** and **B** to the products, dictates the product distribution. If the transition state from the higher energy intermediate is lower than the transition state from the lower energy intermediates, the higher energy intermediate is responsible for product formation (this is typically referred to as the Curtin-Hammett scenario). Although the latter scenario is often invoked to account for a particular (stereochemical) outcome, there is often little quantitative evidence to explain this kinetic pathway, and it is exceedingly difficult to predict such a Curtin-Hammett pathway beforehand. This presents an enormous challenge in the development of stereoselective glycosylation methodologies.

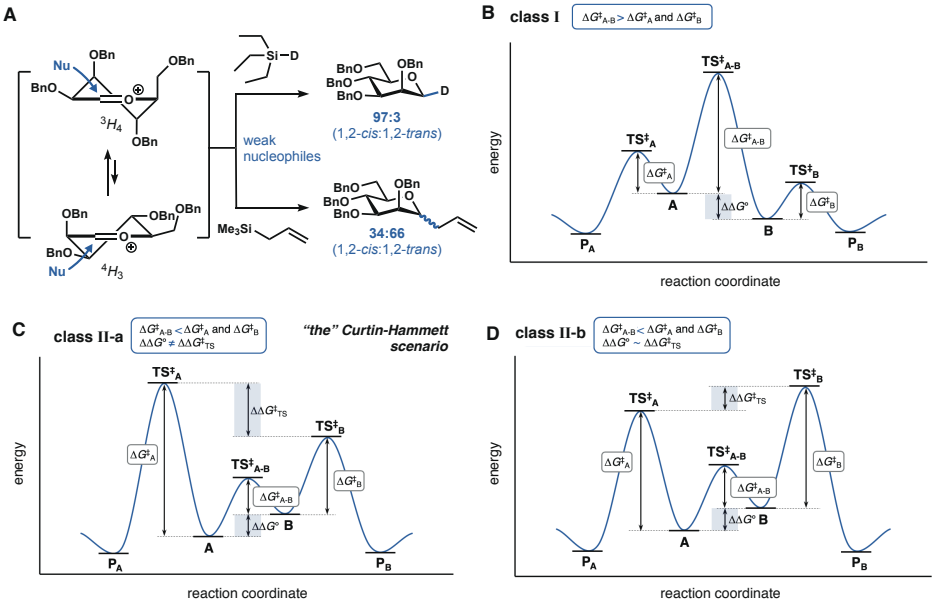


Figure 1. Curtin-Hammett scenarios for the addition of the nucleophile to the glycosyl oxocarbenium ion. (A) Experimentally found Curtin-Hammett scenario, in which two typical S_N1-like nucleophiles, including, allyltrimethylsilane and triethylsilane-*d*, give contrasting stereoselectivities; (B) Curtin-Hammett scenario class I, in which the barrier for interconversion between the reactive species is higher compared to the barrier of addition; (C) and (D) Curtin-Hammett scenario class II-a and II-b, in which the barrier for the addition is higher compared to the interconversion.

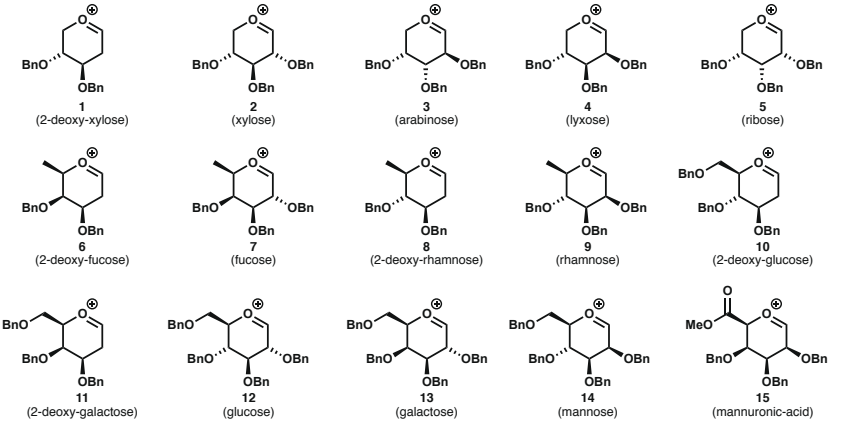
This chapter reports on a study to dissect the Curtin-Hammett scenarios at play during addition reactions to glycosyl cations. It is shown that many of the reactions reported in Chapter 2 proceed via an addition reaction following a barrierless pathway from the intermediate oxocarbenium ions (*i.e.*, class I, Figure 1B). For a selection of reactions, addition reaction barriers were found. In these cases, the relative stability of the oxocarbenium ion conformers cannot account for the stereochemical outcome of the addition reactions, and in-depth transition state analyses revealed the factors that determine the relative energies of the reaction barriers involved. By the use of the activation strain model (ASM) of reactivity and Kohn-Sham molecular orbital (KS-MO) theory, in combination with the matching energy decomposition analysis (EDA), a quantitative description of the various physical factors that control, and distinguish, the addition reactions, is provided. These analyses have revealed the origin of the stereoselectivity of reactions taking place following Curtin-Hammett scenarios of class II (Figure 1C and 1D).

Results and discussion

To investigate the addition reaction to glycosyl cations, a panel of 15 popular glycosyl donors, systematically differing in the number of substituents and their stereochemistry, were subjected to a series of glycosylation reactions with two typical S_N1 nucleophiles: triethylsilane-*d* (TES-*d*)[18,36,37] and allyltrimethylsilane (allyl-TMS). Table 1 summarizes the observed stereoselectivity of the experimental reactions of the thioglycoside donors, obtained by pre-activation of the donors using the diphenyl sulfoxide (Ph_2SO)/triflic anhydride (Tf_2O) activator.[38] Table 1 also reports the theoretical stereochemical preference of the corresponding glycosyl cation based on their conformational preference, established as described in Chapter 2.

As can be seen from Table 1, the majority of the reactions (Table 1, Entry 1-7, 11-13 and 15) proceeds with a similar stereoselectivity for both nucleophiles. In all these cases, the theoretical stereochemical outcome, determined from the population of the different oxocarbenium ion conformational states, matches the stereochemical outcome of the addition reactions. The stereochemical outcome of the addition reactions to oxocarbenium ions **8**-**10** and **14** (Table 1, Entry 8-10 and 14; marked blue) differs for the two nucleophiles (*i.e.*, TES-*d* and allyl-TMS). Of note, all these cations share the same stereochemistry at C3-, C4- and C5-position and can be regarded as belonging to the mannosyl-like series, showing a preference for the formation of *trans*-products when allyl-TMS is used, and a preference for *cis*-products when TES-*d* is used.

Table 1. Computed and experimentally found stereoselectivity for *d*- and *C*-glycosylation reactions on glycosyl cations. For the 2-deoxy-glycosides (Entry 1, 6, 8, 10 and 11) the *cis*:*trans* ratio is expressed as the relationship between the substituent on the C3-position and the coupled nucleophile; for the other glycopyranosides (Entry 2-5, 7, 9 and 12-15) the *cis*:*trans* ratio is expressed as the relationship between the substituent on the C2-position and the coupled nucleophile. For the computational studies, per-*O*-methylated oxocarbenium ions were used, where the experimental glycosylation used per-*O*-benzylated substrates. The generation of all computed data is described in Chapter 2 and based on the CEL map calculations. In cases where the allyl-TMS and TES-*d* results do not match, the entry is marked blue. All glycosyl cations are depicted as their D-analogue for ease of comparison, but cations **6-9** were used as L-sugars.



Entry	glycosyl cation	*experimental* allyltrimethylsilane (allyl-TMS)	*experimental* triethylsilane-*d* (TES-*d*)	*computed* glycosyl cation
1	**1**	>98:2	>98:2	>98:2
2	**2**	>98:2	>98:2	>98:2
3	**3**	>98:2	>98:2	>98:2
4	**4**	>98:2	>98:2	>98:2
5	**5**	>98:2	>98:2	>98:2
6	**6**	<2:98	<2:98	<2:98
7	**7**	>98:2	>98:2	>98:2
8	**8**	9:91	66:34	71:29
9	**9**	23:77	>98:2	>98:2
10	**10**	<2:98	52:48	52:48
11	**11**	<2:98	<2:98	<2:98
12	**12**	>98:2	>98:2	>98:2
13	**13**	>98:2	>98:2	>98:2
14	**14**	34:66	97:3	97:3
15	**15**	>98:2	>98:2	>98:2

While for TES-*d* the stereoselectivity matches well with the computed selectivities, the observed stereoselectivity for the allyl-TMS additions cannot simply be rationalized based on the relative ground state energy of the different oxocarbenium ion conformers.

Thus, to understand the differences in stereochemical outcome, a series of DFT computations were performed to study the transition states of the addition reactions to the oxocarbenium ions, following the approach graphically depicted in Figure 2. All computations were performed by utilizing the B3LYP exchange-correlation (XC) functional[39,40] with a 6-311G(d,p) basis set. Solvation effects of CH_2Cl_2 were taken into account using a polarizable continuum model (For more information see Supplementary Information).[41]

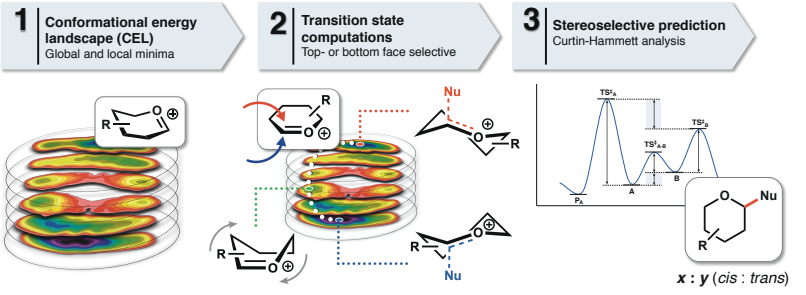


Figure 2. Overview of the workflow to map the stereoselective preference of six-membered ring oxocarbenium ions. (1) The complete conformational space of a six membered ring was scanned by computing 729 pre-fixed structures. The associated energies were graphed on slices dividing the Cremer-Pople sphere; (2) Low energy top- and bottom face selective conformers are selected as initial structure to search for relevant transition states, and relevant conformational transition states were selected which connect the top the bottom of the CEL map; (3) Based on the Curtin-Hammett analysis, the stereochemical outcome of addition reactions to oxocarbenium ions can be computed.

Based on the conformational energy landscape (CEL) maps, generation of which is outlined in Chapter 2 (Figure 2-1), the relevant low-energy conformations of the glycosyl cations were selected for further transition state analysis.[18] Chapter 2 revealed two families of structures to be most relevant: the continuum of (^3E, $^3H_4$, E_4, and $B_{2,5}$)-like structures that are preferentially attacked from the top face, and the 'opposite' family of structures, composed of the (^4E, $^4H_3$, E_3, and $^{2,5}B$)-like conformers, which are likely to be approached by an incoming nucleophile from the bottom face. To find relevant transition states, the two lowest energy structures were selected for each cation, including a conformer from the top face selective family, and a conformer from the bottom face selective family (Figure 2-2). Computationally, the nucleophile was brought closer to the cation in a step-wise manner to find a saddle point on the generated potential energy surface, which was used as a starting point for the TS search. This scan was only performed for the reaction pathways leading to a chair-like TS, since this is the most relevant reaction path (see SI for a detailed study on the diastereotopic selectivity of both allyl-TMS and TES-H additions leading to chair-like

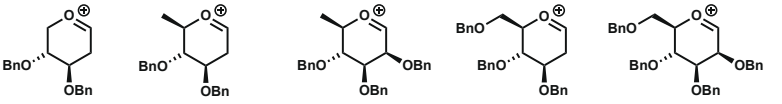
and skew boat TSs; Figure S2-S4). The transition state for the conformational change from the top face selective-structure to the bottom face selective structure was also computed. For these transition state structures, the initial structure for optimization, was provided by the CEL maps, by selecting the saddle point along the conformer interconversion itinerary from the top to the bottom part of the CEL map. These initial TS structures were optimized to find a stationary point, which is verified by performing a vibrational analysis. The character of the normal mode associated with the imaginary frequency of the transition state was analyzed to ensure that it is associated with the reaction of interest. Based on the obtained transition states, the respective reaction profiles were constructed and used to perform a Curtin-Hammett analysis to understand the stereochemical outcome of the addition reactions.

To put this workflow to practice, the addition reaction of TES-H to the 15 glycosyl cations (Table 1) was computed. For the majority of the glycosyl cations, including cations **2-7, 9**, and **12-15**, it was found that the addition of the nucleophile followed a barrierless pathway forming the product complex. These barrierless reactions can be attributed to the very high reactivity of these reactive intermediates. For these cations, formation of the oxocarbenium ions thus represents the reaction's TS and the relative energy levels of these ions is predictive for the stereochemical outcome of the reactions, involving these cations. A Curtin-Hammett class I scenario applies to these ions and the oxocarbenium ion CEL maps generated can be used to rationalize the stereochemical outcome of the triethylsilane additions to these ions.

For cations **1**, **8**, **10** and **11** a TS for the addition was found, which was higher than the interconversion barrier between the top and bottom face selective conformers (see SI for all TS structures; Figure S1). For oxocarbenium ions **1**, **8**, and **10**, the energy levels for the ground state oxocarbenium ion conformers, the barrier for their interconversion ($\Delta G^{\ddagger}_{conf}$), and the computed energy levels of the TS for the top and bottom face additions are summarized in Table 2 (for the analysis of cation **11** see SI; Table S2; not included in the main-text to keep the analysis concise). No significant deviation was found from the "intrinsic" preference of the cations for the addition reaction of TES-H in terms of stereoselectivity, which is completely in line with the experimental results. For 2-deoxy xylosyl cation **1**, the $^{3}H_{4}$ conformer is the most stable oxocarbenium ion because the *O*-substituents on the C3- and C4-position are placed in an axial position, which stabilizes the glycosyl cation through electrostatic interaction.[1,18,29,30] This conformation is 3.2 kcal mol^{-1} more stable than the 'opposite' $^{4}H_{3}$ structure, and the interconversion barrier for the cation is 7.0 kcal mol^{-1}. The TS leading to the addition products from both conformers are found at 9.9 kcal mol^{-1} (top face; $^{3}H_{4}$) and 13.4 kcal mol^{-1} (bottom face; $^{4}H_{3}$). The large difference in energy of these addition TSs ($\Delta\Delta G^{\ddagger}_{addition}$ = –3.5 kcal mol^{-1}) accounts for the stereoselectivity found in the addition reaction (*cis*:*trans* = >98:2), and in this case a Curtin-

Hammett scenario of class II-b applies. A similar analysis holds for oxocarbenium ion **8** and **10**. The difference in kinetic scenarios for the reactions of **8** and **10** and their C2-alkoxy counterparts **9** and **14**, that react with TES-H following a barrierless reaction path, can be explained by the electron withdrawing effect of the C2-alkoxy groups, which destabilize cations **9** and **10**, and which are therefore more reactive than **8** and **10**.

Table 2. Computed and experimentally found stereoselectivity for *d*- and *C*-glycosylation reactions on glycosyl cations. For the 2-deoxy-glycosides the *cis*:*trans* ratio is expressed as the relationship between the substituent on C3-position and the coupled nucleophile; for the other glycopyranoside the *cis*:*trans* ratio is expressed as the relationship between the substituent on C2-position and the coupled nucleophile. For the computational studies, per-*O*-methylated oxocarbenium ions were used, where the experimental glycosylation used per-*O*-benzylated substrates. All data computed at PCM(CH_2Cl_2)-B3LYP/6-311G(d,p). All relative energies ($\Delta\Delta G$) are reported with respect to the conversion of $^4H_3 \rightarrow {}^3H_4$, therefore $\Delta\Delta G°$ is expressed as $\Delta\Delta G° = \Delta G°_{^3H_4} - \Delta G°_{^4H_3}$, the $\Delta\Delta G^‡_{addition}$ is expressed as $\Delta\Delta G^‡_{addition} = \Delta G^‡_{top} - \Delta G^‡_{bottom}$. Both $\Delta G^‡_{top}$ and $\Delta G^‡_{bottom}$ are relative to the lowest-energy conformer.[42,43] All glycosyl cations are depicted as their D-analogue for ease of comparison, but cation **8** and **9** were used as L-sugars. [a] Nonexistent: encounter of reactants induces addition reaction without barrier; [b] Barrierless addition was found, therefore the computed stereoselectivity is based on the conformational preference of the cation (*i.e.*, CEL map).



	3	8	9	10	14
Glycosyl cation					
$\Delta G°_{^3H_4}$	0.0	0.0	0.0	0.0	0.0
$\Delta G°_{^4H_3}$	3.2	0.6	3.1	0.2	1.9
$\Delta\Delta G°$	−3.2	−0.6	−3.1	−0.2	−1.9
$\Delta G^‡_{conf}$	7.0	2.9	3.6	2.7	2.6
triethylsilane (TES-d/H) addition					
exp.	**>98:2**	**66:34**	**>98:2**	**52:48**	**97:3**
$\Delta G^‡_{top}$	9.9	11.1	[a]	10.9	[a]
$\Delta G^‡_{bottom}$	13.4	11.5	[a]	10.6	[a]
$\Delta\Delta G^‡_{addition}$	−3.5	−0.4	[a]	0.3	[a]
comp.	**>98:2**	**72:28**	**>98:2**[b]	**33:67**	**>98:2**[b]
allyltrimethylsilane (allyl-TMS) addition					
exp.	**>98:2**	**9:91**	**23:77**	**<2:98**	**34:66**
$\Delta G^‡_{top}$	10.4	12.9	7.5	11.9	9.6
$\Delta G^‡_{bottom}$	12.8	11.8	6.9	10.7	9.4
$\Delta\Delta G^‡$	−2.4	1.1	0.6	1.2	0.2
comp.	**>98:2**	**7:93**	**20:80**	**5:95**	**38:62**

For the reactions with allyl-TMS, a weaker nucleophile (Mayr's reactivity parameters: $N_{TES\text{-}H} = 3.58$; $N_{allyl\text{-}TMS} = 1.68$)[44] than triethylsilane, barrierless addition reactions were found for oxocarbenium ions **2-7**, **12**, **13** and **15**, proceeding via a Curtin-Hammett scenario of class I. For the other cations (**1**, **8-11** and **14**), TSs were found for the addition reactions that were higher than the barrier for interconversion of the oxocarbenium ion conformers (see Table 2; Figure 3B and 3C shows reaction profiles of representative examples). The addition TSs were slightly higher in terms of energy compared to those that were found for triethylsilane. Notably, again all these cations, barred one (*i.e.*, cation **11**), have the *manno*-like stereochemistry and clear structure-reactivity-selectivity principles can be derived from this series. The substituents at the C3 and C4-position in *manno*-configured oxocarbenium ions can adopt an axial orientation when the ion takes up a $^3H_4$-half chair conformation (here the mannopyranose structures in the D-series will be used; Figure 3A). As discussed above, the electrostatic stabilization by the substituents on the cation overrides the steric preference of the substituents, however with an increasing number of substituents and a weaker nucleophile (*i.e.*, late TS), one can imagine that steric interactions become important and counterbalance the "intrinsic" preference of the cations (Figure 3A). In almost all cases deviation was found from the "intrinsic" preference of the cations (except cation **1**) for the addition reaction of Allyl-TMS in terms of stereoselectivity, which is completely in line with the experimental results.

For 2-deoxy-xylosyl cation **1**, the addition of allyl-TMS preferentially occurs from the top face on the $^3H_4$-ion, in line with triethylsilane, via a TS structure corresponding to a barrier height of 10.4 kcal mol^{-1}. The TS for attack on the other side (bottom face; $^4H_3$-cation), however, requires more energy ($\Delta G^{\ddagger}_{bottom}$ = 12.8 kcal mol^{-1}), which expresses itself in the observed stereoselectivity of this addition reaction.

For 2-deoxy rhamnosyl ion **8**, the addition of allyl-TMS results in a 1,3-*trans* selectivity (7:93), in contrast to triethylsilane (72:28; *vide supra*). This can be attributed to the found TSs, which are 12.9 kcal mol^{-1} (top face; $^3H_4$) and 11.8 kcal mol^{-1} (bottom face; $^4H_3$). To understand the shift to more *trans*-product than expected on the basis of the preference of the cation, one can analyze both approaches and can imagine that the top face addition follows a more sterically crowed path (*i.e.*, the more hindered face) as a result of the axial groups in the $^3H_4$ conformation (*i.e.*, C3- and C5-position). This leads to a higher barrier for the late TS of allyl-TMS, and therefore follows a Curtin-Hammett class II-a type scenario. Cation **10** (Figure 3B and 3D) closely resembles 2-deoxy rhamnosyl cation **8**, and thus addition reactions to **10** proceed via a similar kinetic scenario. The difference in stereochemical outcome of the reactions involving triethylsilane and allyl-TMS, and ions **8** and **10** are well accounted for by their differences in $\Delta\Delta G^{\ddagger}_{addition}$. Additionally, the allyl-TMS addition reactions to rhamnosyl cation **9** and mannosyl cation **14** (Figure 3C and 3E), provide more of the β-products (**9** α:β = 77:23; **14** α:β = 66:34) than the addition reactions

to the 2-deoxy cations **8** (α:β = 91:9) and **10** (α:β = <98:2). From Table 2 it becomes apparent that this difference (**9** *vs* **14** and **8** *vs* **10**) can be related to the larger difference in ground state energy of the $^{3}H_{4}$- *vs* the $^{4}H_{3}$-half chair conformers for the C2-alkoxy cations, favoring the former conformation. The more reactive cations **9** and **14**, with respect to ions **8** and **10**, lead to lower activation barriers for the former ions. In line with the kinetic scenarios for the allyl-TMS addition reactions to **8** and **10**, the reactions of **9** and **14** with allyl-TMS can be described by a Curtin-Hammett II-a scenario.

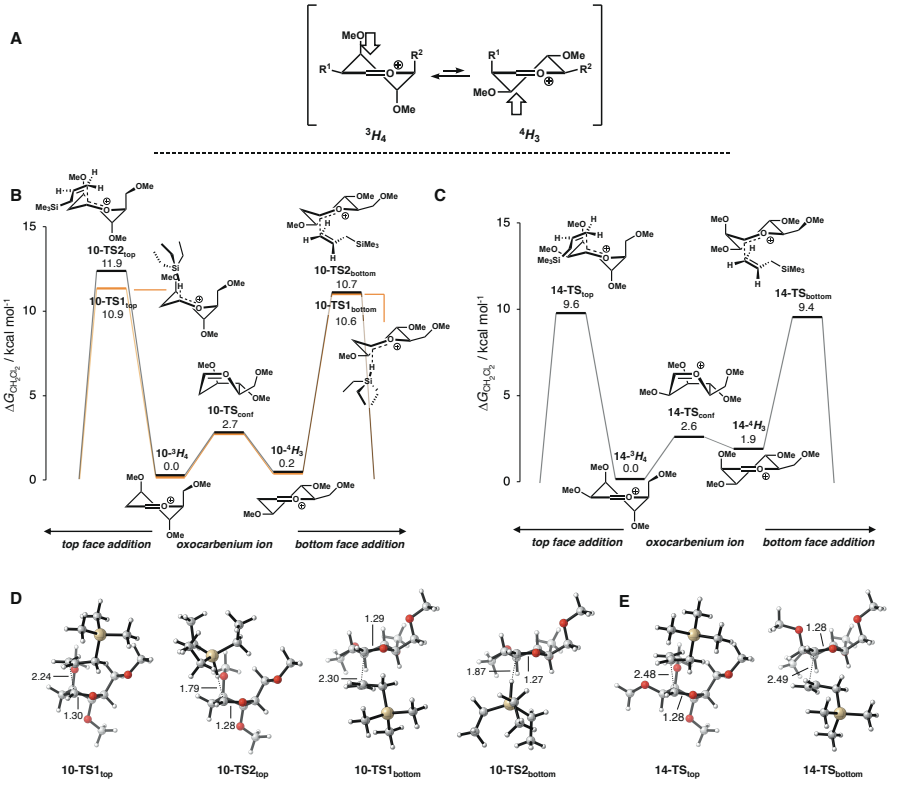


Figure 3. Selected reaction profiles for addition reactions to glycosyl cations. (A) Simplified conformational equilibrium of *manno*-like configured glycosyl cations, and the direction of the incoming nucleophile; R^1 = H or OMe/OBn and R^2 = H or CH_2OMe/CH_2OBn; Reaction profiles for the allyl-TMS (black) and TES-H (orange) addition at cation **10** (B) and **14** (C); Transition state structures with key bond lengths (in Å) for cation **10** (D) and **14** (E). Computed at PCM(CH_2Cl_2)-B3LYP/6-311G(d,p).

Overall, the computed activation barriers excellently explain the differences in stereochemistry of the triethylsilane and allyl-TMS additions. The computational analysis of the stability and conformational behavior of the oxocarbenium ion conformers, using the CEL mapping method, combined with the quantitative analyses of the activation barriers for the addition reactions to the cations, provides an accurate description of the

different Curtin-Hammett type kinetic scenarios that operate during addition reactions to substituted pyranosyl oxocarbenium ions.

To understand why the addition reactions with allyl-TMS deviate from the "intrinsic" preference imposed by the stability of the cations and follow Curtin-Hammett type kinetic scenarios, the activation strain model (ASM)[45–50] of reactivity was applied in the gas-phase (see SI for computational method). First, the addition reaction of allyl-TMS to **1**, **8**, **10** and **14** was studied. The ASM allows one to decompose the solution-phase potential energy surface, *i.e.*, total energy of the reacting components ($\Delta E(\zeta)$) along the reaction pathway, into the total strain and interaction energy, $\Delta E_{\text{strain}}(\zeta)$ and $\Delta E_{\text{int}}(\zeta)$, respectively. Herein, the total strain energy, $\Delta E_{\text{strain}}(\zeta)$, is the penalty that needs to be paid in order to deform the individual reactants from their equilibrium structure to the geometry they adopt during the reaction at point ζ along the reaction coordinate. The interaction energy, $\Delta E_{\text{int}}(\zeta)$, accounts for all the mutual interactions that occur between these two deformed reactants. In this study, the energy terms are projected on the stretch of the C=O$^+$ (C1–O5) bond, which lengthens as the reactions progresses. This critical reaction coordinate undergoes a well-defined change during the addition reaction from the reactants via the transition state to the product.[51–53]

The interaction energy can be further decomposed using the energy decomposition analysis (EDA)[54–56] scheme, which dissects the $\Delta E_{\text{int}}(\zeta)$ into three physically meaningful energy terms, namely, (i) the electrostatic interactions between the unperturbed charge distribution of the deformed reactants: $\Delta V_{\text{elstat}}(\zeta)$; (ii) the destabilizing Pauli repulsion between the overlapping occupied-occupied closed-shell orbitals of both fragments due to the Pauli principle (*i.e.*, steric interactions), $\Delta E_{\text{Pauli}}(\zeta)$; and (iii) the stabilizing orbital interactions, which account for polarization and charge transfer between the fragments, such as HOMO–LUMO interactions, $\Delta E_{\text{oi}}(\zeta)$. Thus, the combined ASM/EDA approach allows the quantitative assessment of all physical factors that influence the total energy of a reaction path and its transition state, and hence can be used to quantify the intrinsic differences between chemical reactions.

Figure 4 displays the ASM/EDA analyses for the addition of allyl-TMS to both the $^3H_4$ and $^4H_3$-conformer of **1**, **8**, **10** and **14**. Figure 4A (left panel) shows the ASM results of the 2-deoxy-xylosyl cation **1**, in which the lower activation barrier for the top face attack (black line) compared to the bottom face attack (red line) exclusively originates from a less destabilizing strain energy (lower ΔE_{strain} curve at the same ζ). By decomposing the total strain energy term into the strain energy of the individual reactants (SI Figure S5), it was found that the less destabilizing strain energy of the top face attack can mainly be attributed to the "intrinsic" stability of the $^3H_4$-cation **1**, which is 3.2 kcal mol^{-1} more stable than its $^4H_3$-counterpart (see Table 2).

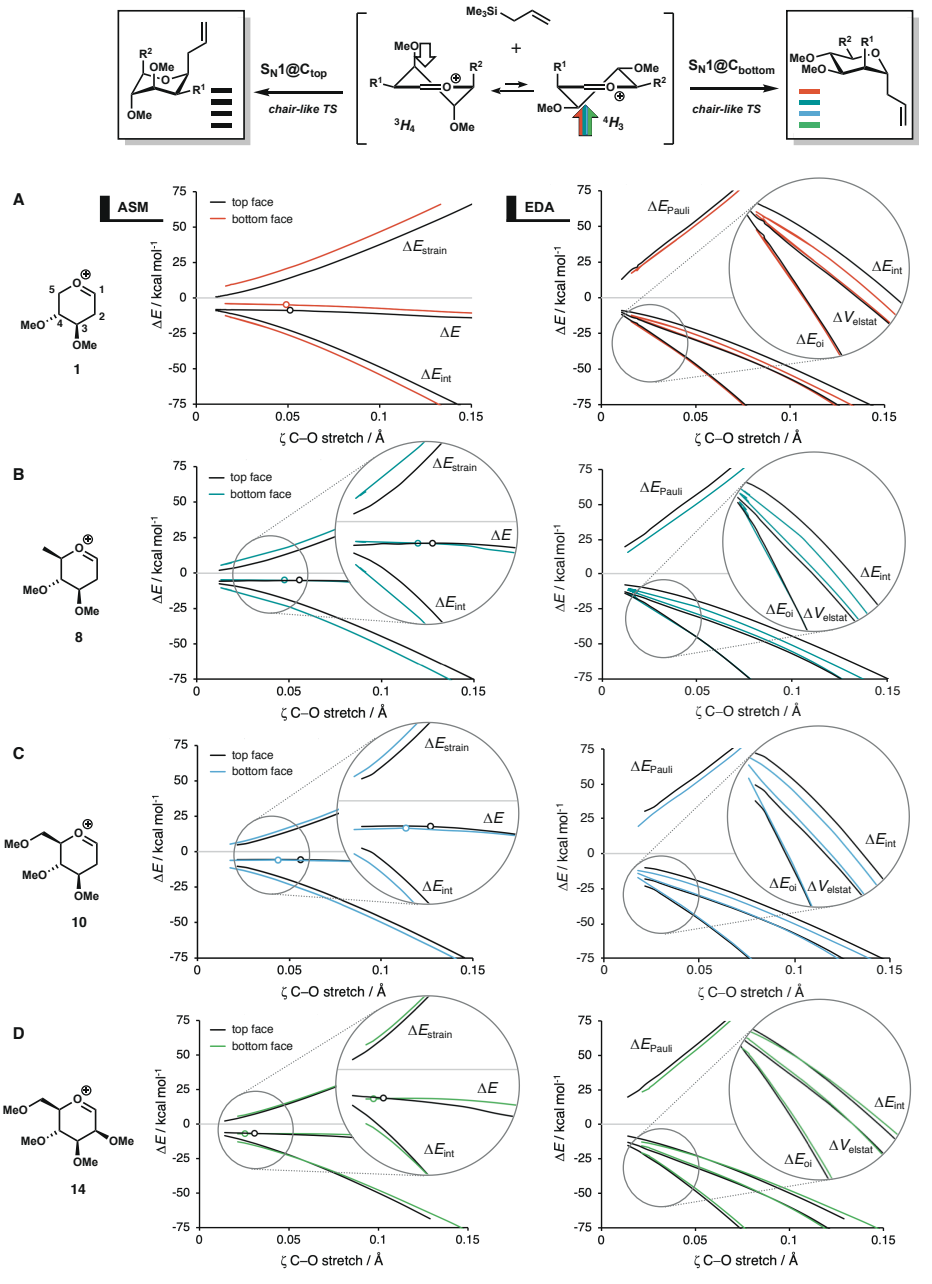


Figure 4. Activation strain analysis (left) and energy decomposition analysis (right) of the allyl-TMS addition reaction of cation **1**, **8**, **10** and **14** (top face = black; bottom face = red/purple/blue/green), where the energy values are projected on the C–O stretch. R^1 = H or OMe and R^2 = H, Me or CH_2OMe. TSs are indicated by dots; Computed in the gas-phase at ZORA-B3LYP/TZ2P//PCM(CH_2Cl_2)-B3LYP/6-311G(d,p).

The addition at both faces (top and bottom face) follows a similar reaction path, through a chair-like transition state, which is reflected in a similar strain energy path, only the offset is different as a result of the intrinsic stability of the conformation of the cations. This behavior can be found for all computed cations, thus the strain is always less destabilizing for the more stable conformer, *i.e.*, the conformer with more axial electron-rich substituents at distal positions ($^3H_4$ conformer). As discussed above, the axial orientated substituents at the C3- and C4-position are able to stabilize the cation by electrostatic interactions (see Table S5 and Figure S11).[1,18,29,30]

In contrast, for cations **8**, **10** and **14** (Figure 4B-D), the bottom face attack is favored, which originates solely from a more stabilizing interaction energy. For these cations, the strain energy is, as above described, less destabilizing for the top face attack, however, the difference with the bottom face attack is significantly less compared to cation **1**, and therefore the interaction energy controls the face selectivity. This can be traced back to the relatively small energy difference between the $^3H_4$- and $^4H_3$-conformer for these cations (see Table 2). For all cations (**1**, **8**, **10** and **14**), the interaction energy is always more stabilizing for the conformer with lowest number of axial electron-rich substituents at distal positions (*i.e.*, $^4H_3$ conformer).

In order to understand the origin of the more stabilizing interaction energy for the bottom face attack, an EDA was performed, and the results are depicted in Figure 4B-D (right panel). In all cases the difference in interaction energy can be traced to the Pauli repulsion, with the other terms (*i.e.*, ΔE_{oi} and ΔV_{elstat}) being almost equal for the top and bottom face attack. The more destabilizing Pauli repulsion for the top face attack can be directly traced back to the axial groups (C3- and C5-position) present in the $^3H_4$ conformation, which cause steric interactions with the incoming allyl-TMS (Figure 5; see SI for Kohn-Sham molecular orbital analysis and double consistent geometries).

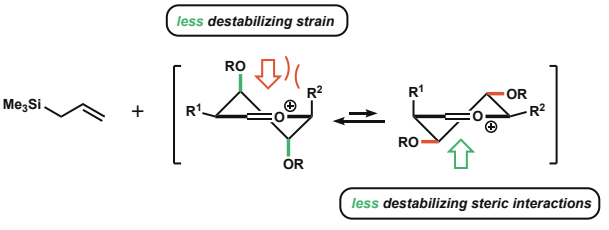


Figure 5. Schematic representation of the controlling factors (green = stabilizing; red = destabilizing factors) of the stereoselectivity of *C*-glycosylation reactions, in which the strain is always less destabilizing for the more stable conformer (*i.e.*,$^3H_4$), while the Pauli repulsion is also always more destabilizing for this conformation; R^1 = H or OBn and R^2 = H, Me or CH_2OBn.

From the activation strain and energy decomposition analysis, it can be concluded for *C*-glycosylations that the strain is always less destabilizing for the more stable conformer, while the Pauli repulsion is also always more destabilizing for this conformation (Figure 5), and the magnitude of both effects will ultimately determine the face selectivity: (i) for the "stripped" model glycosyl cation **1**, a regime of strong "intrinsic" conformational preference can be found, in which the strain determines the face selectivity, and this is more favored for the conformer with the most axial electron-rich substituents at distal positions; (ii) for the more decorated cations **8**, **10** and **14**, a regime of weak "intrinsic" preference of the cation can be found, in which the interaction energy determines the face selectivity, and this results in an addition at the least hindered face as a result of a less destabilizing (steric) Pauli repulsion with allyl-TMS.

To understand the contrasting behavior between allyl-TMS and TES-*d*, in which TES-*d* does follow the "intrinsic" preference of the cations, a similar analysis for the addition reactions of TES-H to cation **1** and **10** (see SI for the analysis; Figure S9 and S10) was performed. The addition of TES-H proceeds following a reaction path having a significantly earlier TS (*i.e.*, less C–O bond stretch), because of the higher nucleophilicity of triethylsilane.[33] These early TSs resemble more closely the reactants (*i.e.*, the glycosyl cation), in which steric interactions play a minor role. Indeed, the difference in Pauli repulsion for both faces in an early TS (*i.e.*, Nuc is relatively far away from the electrophile) is smaller, which cause the strain to take full control (*i.e.*, "intrinsic" preference of the cation).

Overall, the ASM-EDA analyses provide a quantitative description of the various physical factors that control the addition reactions on the different oxocarbenium ion conformers, allowing for an accurate and well substantiated description of Curtin-Hammett kinetic scenarios at play.

Conclusion

In conclusion, in this chapter different kinetic scenarios were mapped through which S_N1-type addition reactions of six-membered ring glycosyl oxocarbenium ions can proceed. A combined computational and experimental approach has unraveled how the reactivity of oxocarbenium ions, governed by the substitution pattern on the carbohydrate ring, in combination with the reactivity of the incoming nucleophile, determines the stereochemical outcome of the S_N1-type addition reactions. Using the conformational energy landscape (CEL) maps different low energy oxocarbenium ion conformers were selected, which were used as a starting point to find transition states for addition reactions taking place by a top or bottom face attack of the nucleophile. Using the stability of the

different oxocarbenium ion conformers, the barrier for their interconversion and addition, possible Curtin-Hammett kinetic scenarios have been dissected.

It has been shown that many addition reactions with triethylsilane proceed with a barrierless pathway, from the high energy – but relatively stable – oxocarbenium ion conformers to the products. For these cations the population of conformational families with a preference for top or bottom face attack provides an adequate explanation for the stereochemistry observed in reactions of these cations. Reactions of the weaker nucleophile, allyl-TMS, with relatively stable oxocarbenium ions, such as those having the *manno*-configuration, a Curtin-Hammett kinetic scenario takes effect. A reaction path with a barrier is followed and for these reactions the relative energy level of transition states of the top and bottom face addition is decisive in determining the stereochemical outcome.

By using the activation strain analysis, a quantitative description of the factors influencing the stereoselectivity could be provided, and revealed how the interplay between the oxocarbenium ion stability, and the build-up of (steric) Pauli repulsion along the reaction, and the position of the transition state along the reaction coordinate, dictate the height of the reaction barrier for these addition reactions. For *C*-glycosylations, general guidelines emerged to understand the selectivity: (i) for "stripped" glycosyl cations, a regime of strong "intrinsic" conformational preference can be found, in which the strain determines the face selectivity, and this is more favored for the conformer with the most axial electron-rich substituents at distal positions; (ii) for the more decorated cations, a regime of weak "intrinsic" preference of the cation can be found, in which the interaction energy determines the face selectivity, and this results in an addition at the least hindered face as a result of a less destabilizing (steric) Pauli repulsion with allyl-TMS.

The mechanistic insight offered here will be instrumental in the interpretation of the outcome of glycosylation reactions in the future and serve as the basis to further explore oxocarbenium ions as reactive intermediates and map the effect of various protecting and functional group patterns.

Supporting information

Computation method

Computational details • The density functional theory (DFT) computations were performed using Gaussian 09 rev D.01.[57] For all computation, the hybrid functional B3LYP and the 6-311G(d,p) basis set were used. The geometry convergence criteria were set to tight (opt=tight; max. force=$1.5 \cdot 10^{-7}$, max. displacement=$6.0 \cdot 10^{-7}$), and an internally defined super-fine grid size was used (SCF=tight, int=veryfinegrid), which is a pruned 175,974 grid for first-row atoms and a 250,974 grid for all other atoms. These parameters were chosen as a recent paper indicated a significant dependence of the computed frequencies on the molecule orientation when a smaller grid size is used.[58] Geometries were optimized without symmetry constraints. All calculated stationary points have been verified by performing a vibrational analysis, to be energy minima (no imaginary frequencies) or transition states (only one imaginary frequency). The character of the normal mode associated with the imaginary frequency of the transition state has been analyzed to ensure that it is associated with the reaction of interest. Solvation in CH_2Cl_2 was taken into account in the computations using the PCM implicit solvation model. Solvent effects were explicitly used in the solving of the SCF equations and during the optimization of the geometry and the vibrational analysis. The potential energy surfaces of the studied addition reactions were obtained by performing intrinsic reaction coordinate (IRC) calculations, which, in turn, were analyzed using the PyFrag program (*vide infra*).[59] The optimized structures were illustrated using CYLview.[60]

The denoted free Gibbs energy was calculated using Equation S1, in which ΔE_{gas} is the gas-phase energy (electronic energy), $\Delta G^{T}_{gas,QH}$ (T = 213.15 K, p = 1 atm., C = 1 M) is the sum of corrections from the electronic energy to the free Gibbs energy in the quasi-harmonic oscillator approximation, including zero-point-vibrational energy, and ΔG_{solv} is their corresponding free solvation Gibbs energy. The $\Delta G^{T}_{gas,QH}$ was computed using the quasi-harmonic approximation in the gas phase according to the work of Truhlar. The quasi-harmonic approximation is the same as the harmonic oscillator approximation except that vibrational frequencies lower than 100 cm^{-1} were raised to 100 cm^{-1} as a way to correct for the breakdown of the harmonic oscillator model for the free energies of low-frequency vibrational modes.[61]

$$\Delta G^{T}_{CH_2Cl_2} = \Delta E_{gas} + \Delta G^{T}_{gas,QH} + \Delta G_{solv} = \Delta G^{T}_{gas} + \Delta G_{solv} \quad \text{(Eq. S1)}$$

Activation strain and energy decomposition analysis • The activation strain model (ASM) analysis and energy decomposition analysis (EDA) were performed using the Amsterdam Density Functional (ADF2017.103)[62–64] software package based on the solution-phase structures obtained by Gaussian 09. For all computations, the B3LYP functional was used. The basis set used, denoted TZ2P, is of triple-ζ quality for all atoms and has been improved by two sets of polarization functions.[65] The accuracies of the fit scheme (Zlm fit) and the integration grid (Becke grid) were, for all calculations, set to VERYGOOD.[66,67] Relativistic effects were accounted for by using the zeroth-order regular approximation (ZORA).[68,69] All computations were performed in the gas-phase on the obtained solution-phase structures (*vide infra*).

The activation strain model (ASM) of chemical reactivity[45–48], also known as the distortion/interaction model[49,50], is a fragment-based approach in which the energy corresponding to a chemical reaction, *i.e.*, potential energy surface, can be described with respect to, and understood in terms of the characteristics of, the reactants. It considers the rigidity of the reactants as well as to which extent they need to deform during the reaction plus their capability to interact with each other as the reaction proceeds. In this model, the total energy, $\Delta E(\zeta)$, is decomposed into the respective total strain and interaction energy, $\Delta E_{strain}(\zeta)$ and $\Delta E_{int}(\zeta)$, and project these values onto the reaction coordinate ζ (Eq. S2).

$$\Delta E(\zeta) = \Delta E_{strain}(\zeta) + \Delta E_{int}(\zeta) \quad \text{(Eq. S2)}$$

In this equation, the total strain energy, $\Delta E_{strain}(\zeta)$, is the penalty that needs to be paid to deform the reactants from their equilibrium structure to the geometry they adopt during the reaction at point ζ of the reaction coordinate. On the other hand, the interaction energy, $\Delta E_{int}(\zeta)$, accounts for all the chemical interactions that occur between these two deformed reactants along the reaction coordinate. The total strain energy can, in turn, be further decomposed into the strain energies corresponding to the deformation of the glycosyl cation, $\Delta E_{strain,cation}(\zeta)$, as well as from the nucleophile, $\Delta E_{strain,nuc}(\zeta)$ (Eq. S3).

$$\Delta E_{strain}(\zeta) = \Delta E_{strain,cation}(\zeta) + \Delta E_{strain,nuc}(\zeta) \quad \text{(Eq. S3)}$$

In this study, the solution-phase potential energy surface, $\Delta E_{solution}(\zeta)$, was decomposed into the $\Delta E_{solvation}(\zeta)$, which accounts for the interaction between the solute and solvent, and the $\Delta E_{solute}(\zeta)$, which is the reaction system in vacuum with the solution-phase geometry (Eq. S4).[70,71]

$$\Delta E_{solution}(\zeta) = \Delta E_{solvation}(\zeta) + \Delta E_{solute}(\zeta) \quad \text{(Eq. S4)}$$

The solute term, $\Delta E_{solute}(\zeta)$, is subsequently decomposed into the solvent-free strain, $\Delta E_{solute\text{-}train}(\zeta)$, and interaction energy, $\Delta E_{solute\text{-}int}(\zeta)$, which are referred to as solute strain and solute interaction, respectively, to distinguish between the two solution-phase activation strain schemes (Eq. S5).

$$\Delta E_{solution}(\zeta) = \Delta E_{solvation}(\zeta) + \Delta E_{solute\text{-}strain}(\zeta) + \Delta E_{solute\text{-}int}(\zeta) \quad \text{(Eq. S5)}$$

For clarity reasons, ΔE_{solute}, $\Delta E_{solute\text{-}strain}$ and $\Delta E_{solute\text{-}int}$ are denoted as ΔE, ΔE_{strain} and ΔE_{int} in all the result and discussion sections of the main-text and SI.

The interaction energy between the deformed reactants can be further analyzed in terms of quantitative Kohn-Sham molecular orbital theory (KS-MO) together with a canonical energy decomposition analysis (EDA).[54–56] The EDA decomposes the $\Delta E_{solute\text{-}int}(\zeta)$ into the following three physically meaningful energy terms (Eq. S6):

$$\Delta E_{solute\text{-}int}(\zeta) = \Delta V_{elstat}(\zeta) + \Delta E_{Pauli}(\zeta) + \Delta E_{oi}(\zeta) \quad \text{(Eq. S6)}$$

Herein, $\Delta V_{elstat}(\zeta)$ is the classical electrostatic interaction between the unperturbed charge distributions of the (deformed) reactants and is usually attractive. The Pauli repulsion, $\Delta E_{Pauli}(\zeta)$, comprises the destabilizing interaction between occupied closed-shell orbitals of both fragments due to the Pauli principle. The orbital interaction energy, $\Delta E_{oi}(\zeta)$, accounts for polarization and charge transfer between the fragments, such as HOMO–LUMO interactions.

In this study, in both the activation strain diagrams and accompanied energy decomposition plots, the energy terms are projected onto the C–O stretch, unless otherwise stated. This critical reaction coordinate undergoes a well-defined change during the reaction from the reactant via the transition state to the product.[51,52]

Transition state structures

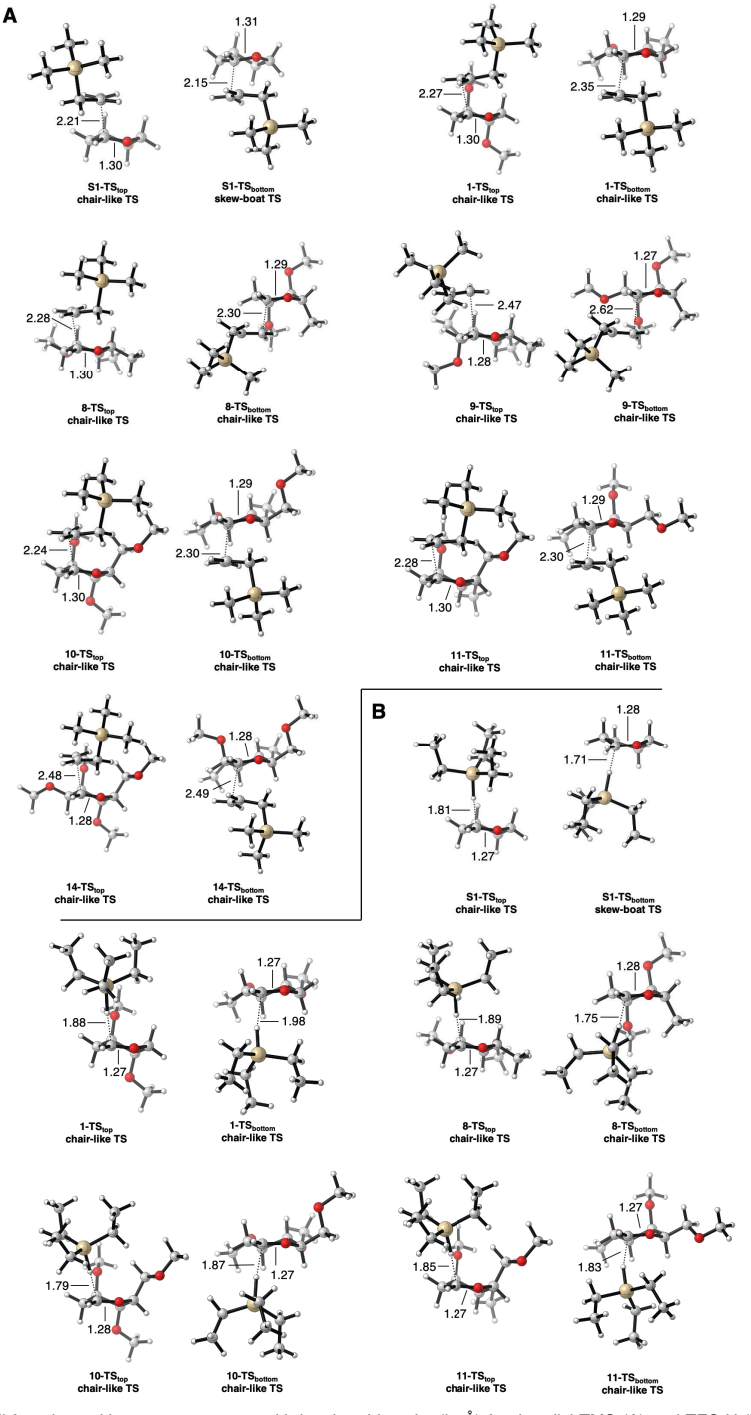


Figure S1. All found transition state structures with key bond lengths (in Å) for the allyl-TMS (A) and TES-H (B) addition reactions for a panel of 15 glycosyl cations. Computed at PCM(CH_2Cl_2)-B3LYP/6-311G(d,p).

Stereotopic face-selectivity • The face selectivity of the addition reaction of both allyl-TMS and triethylsilane at the half-chair conformation of "stripped" model oxocarbenium ion **S1** was computationally studied. The transition state structures of the S_N1-addition reactions with allyl-TMS for the top and bottom face attack at **S1**, as well as their corresponding reactant complex (ΔE_{RC}), electronic activation barriers ($\Delta E^{\ddagger}$), and reaction energies ($\Delta E_{rxn\text{-}int}$) are shown in Figure S2B. The top face addition resulted in a chair-like TS structure (Figure S2C; left structure), while the bottom face addition proceeds through a skew-boat TS (Figure S2C; right structure). As expected, based on the experimental model devised by the group of Woerpel[1,30], it was found that the nucleophilic attack from the top face is favored by more than 3 kcal mol^{-1}.

To gain quantitative insight into the physical factors leading to this face-selectivity, activation strain model (ASM) analysis was performed. By applying the ASM, it was found that the preferred nucleophilic attack at the top face of **S1** originates from a synergetic effect of a more stabilizing interaction energy and a less destabilizing strain energy (Figure S2D). To understand the origin of the less destabilizing strain energy, the total strain energy was decomposed into the strain energies of the separate reactants, according to Equation S3 (Figure S2E). The more stabilizing strain energy of the attack at the top face is exclusively caused by the deformation of glycosyl cation **S1**. When comparing the geometries of the glycosyl cation at consistent geometries with a C–O distance of 0.052 Å stretch (close to the TS for both additions) for the attack at the top and bottom face, it was found that the deformation of the most crucial dihedral angle, $\angle_{C2\text{-}C1\text{-}O5\text{-}C5}$, did not match the observed trend (Figure S2F). Instead, the remaining ring dihedral angles could be attributed to the trend, in which the top face attack (chair-like TS) showed significant less deformation.

To dissect the more stabilizing interaction energy for the top face attack, a canonical energy decomposition analysis (EDA) was performed (Figure S2G). It was established that the trend in ΔE_{int} is predominantly determined by the ΔE_{oi} and ΔV_{elstat}, in which the top face attack has more stabilizing orbital and electrostatic interactions. One might be tempted to conclude that the face-selectivity is determined instead by the less destabilizing Pauli interactions. However, it should be noted that the EDA terms are highly dependent on the Nuc•••C distance (*vide infra*), which is 0.06 Å longer for top face attack compared to bottom face (2.21 Å for top face and 2.15 Å for bottom face) at a C–O bond stretch of 0.052 Å. To remedy this and account for the effect of the different nucleophile–substrate bond distances on the EDA terms, the same consistent geometries were taken, but now the Nuc•••C bond of the top face addition was artificially shortened to the same length as the bottom face attack (see Table S1). This resulted in a more stabilizing ΔE_{oi} and ΔV_{elstat} interaction for the top face attack compared to the bottom face attack (top face: ΔE_{oi} = –56.1 and ΔV_{elstat} = –35.9 kcal mol^{-1}, and bottom face: ΔE_{oi} = –54.5 and ΔV_{elstat} = –33.6 kcal mol^{-1}). Projecting the ASM and EDA on the Nuc•••C distance (see Figure S3C and S3D) supports this, showing significantly more stabilizing ΔE_{oi} and ΔV_{elstat} for the top face addition during the whole reaction path, while the ΔE_{Pauli} is virtually the same.

The same analysis was performed for triethylsilane as the nucleophile, which results in similar trends (Figure S4). The strong face selectivity is maintained, and it again originates from a cooperative effect of a more stabilizing interaction energy and less destabilizing strain (Figure S4D). Importantly, TES-H is a stronger nucleophile compared to allyl-TMS, which results in an earlier transition state (*i.e.*, less C–O stretch at the TS; Figure S4C). This leads to lower overall reaction barriers and TS structures which include significant less deformation of the key dihedral angle, $\angle_{C2\text{-}C1\text{-}O5\text{-}C5}$, compared to the allyl-TMS system. The computational results support that for both nucleophiles the chair-like TS is the most relevant face of attack, and only this approach will be considered in the remaining analysis.

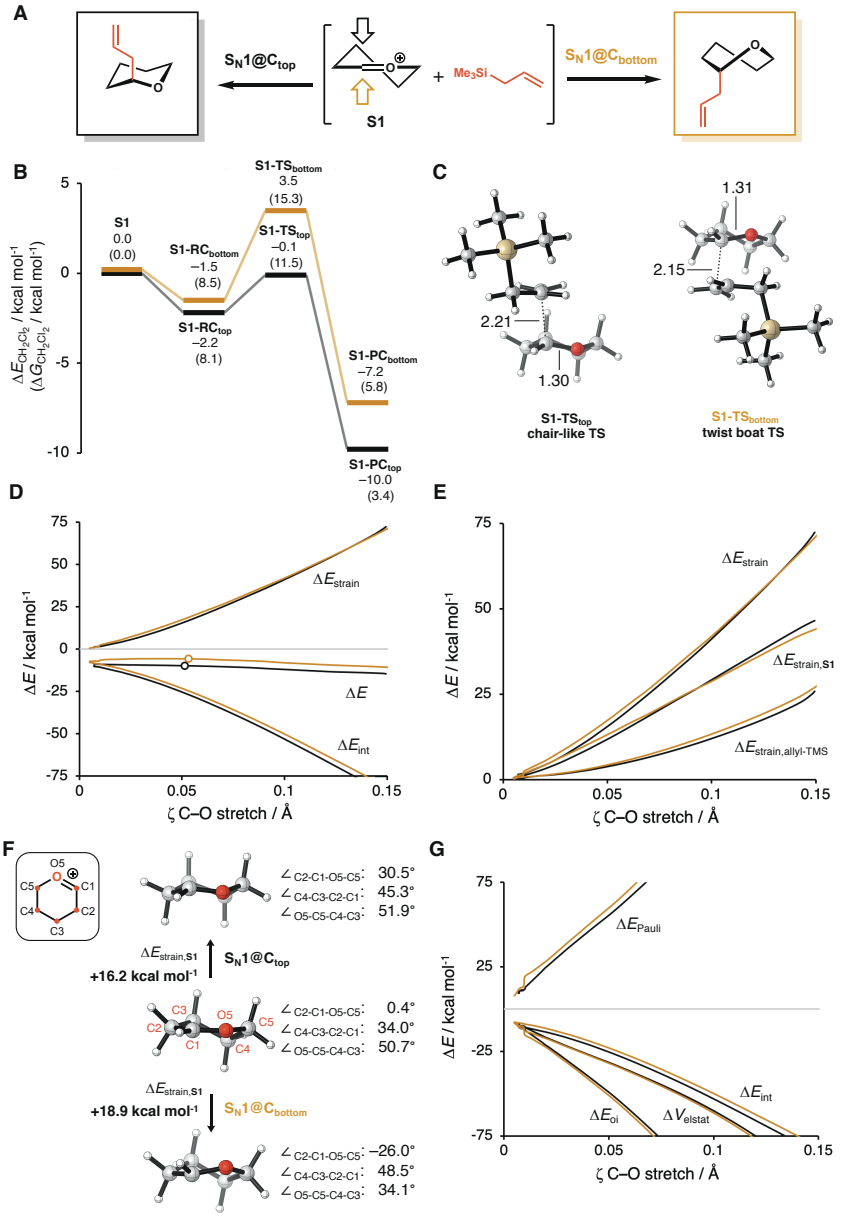


Figure S2. (A) Computationally analyzed allyl-TMS addition reactions of model glycosyl cation **S1**; (B) Reaction profiles for the top and bottom face addition reactions computed at PCM(CH_2Cl_2)-B3LYP/6-311G(d,p) and expressed as $\Delta E_{CH_2Cl_2}$ and $\Delta G_{CH_2Cl_2}$ values in kcal mol^{-1}; (C) The transition state structures with key bond lengths (in Å); (D) Activation strain analysis; (E) Strain decomposition analysis; (F) Deformation of the glycosyl cation upon the attack from the top face and bottom face at consistent geometries with the C–O bond stretch of 0.052 Å; and (G) Energy decomposition analysis of the addition reaction of model glycosyl cation **S1**, where the energy values are projected on the C–O bond stretch; TSs are indicated by dots; Computed in the gas-phase at ZORA-B3LYP/TZ2P//PCM(CH_2Cl_2)-B3LYP/6-311G(d,p).

Table S1. Activation strain and energy decomposition analyses (in kcal mol^{-1}) for the addition reaction at **S1**. Analyses at consistent geometries with a C–O bond stretch of 0.052 Å and a Nuc•••C bond distance of 2.15 Å. Computed at ZORA-B3LYP/TZ2P.

	$\Delta E^{\ddagger}$	ΔE_{strain}	ΔE_{int}	ΔV_{elstat}	ΔE_{Pauli}	ΔE_{oi}
S1$_{top}$	–9.8	16.2	–26.0	–35.9	66.0	–56.1
S1$_{bottom}$	–5.8	18.9	–24.6	–33.6	63.5	–54.5

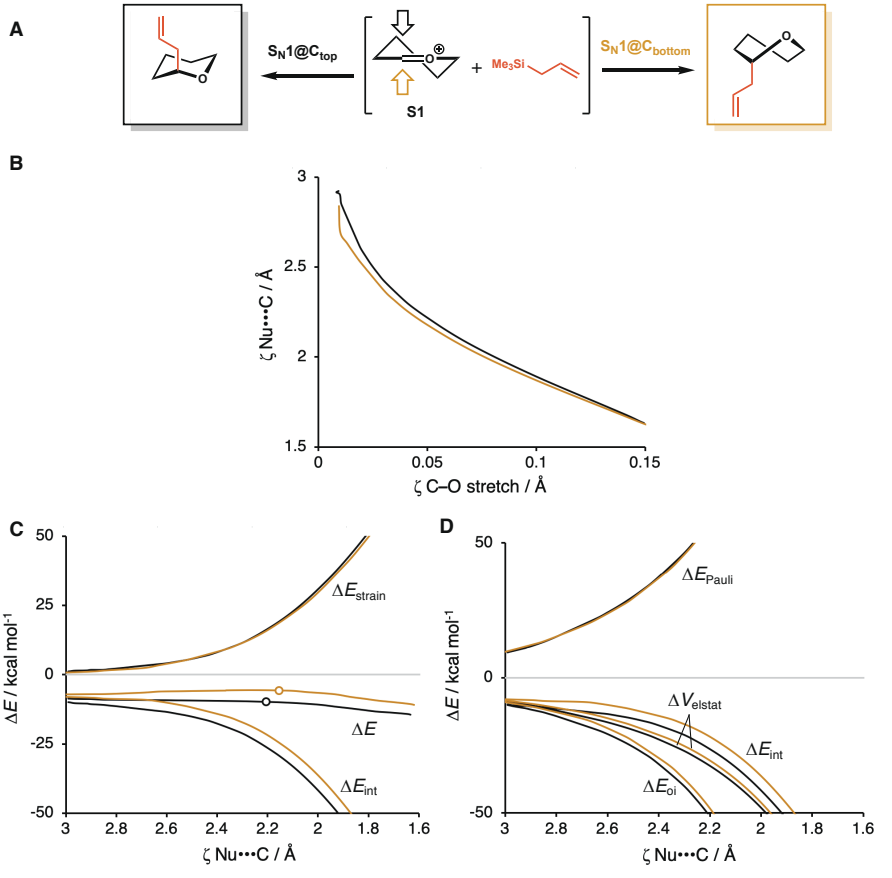


Figure S3. (A) Computationally analyzed allyl-TMS addition reactions of model glycosyl cation **S1**; (B) Nuc•••C distance projected on the C–O bond stretch; (C) Activation strain analysis; and (D) Energy decomposition analysis of the addition reaction of model glycosyl cation **S1**, where the energy values are projected on the Nuc•••C distance; TSs are indicated by dots; Computed in the gas-phase at ZORA-B3LYP/TZ2P//PCM(CH_2Cl_2)-B3LYP/6-311G(d,p).

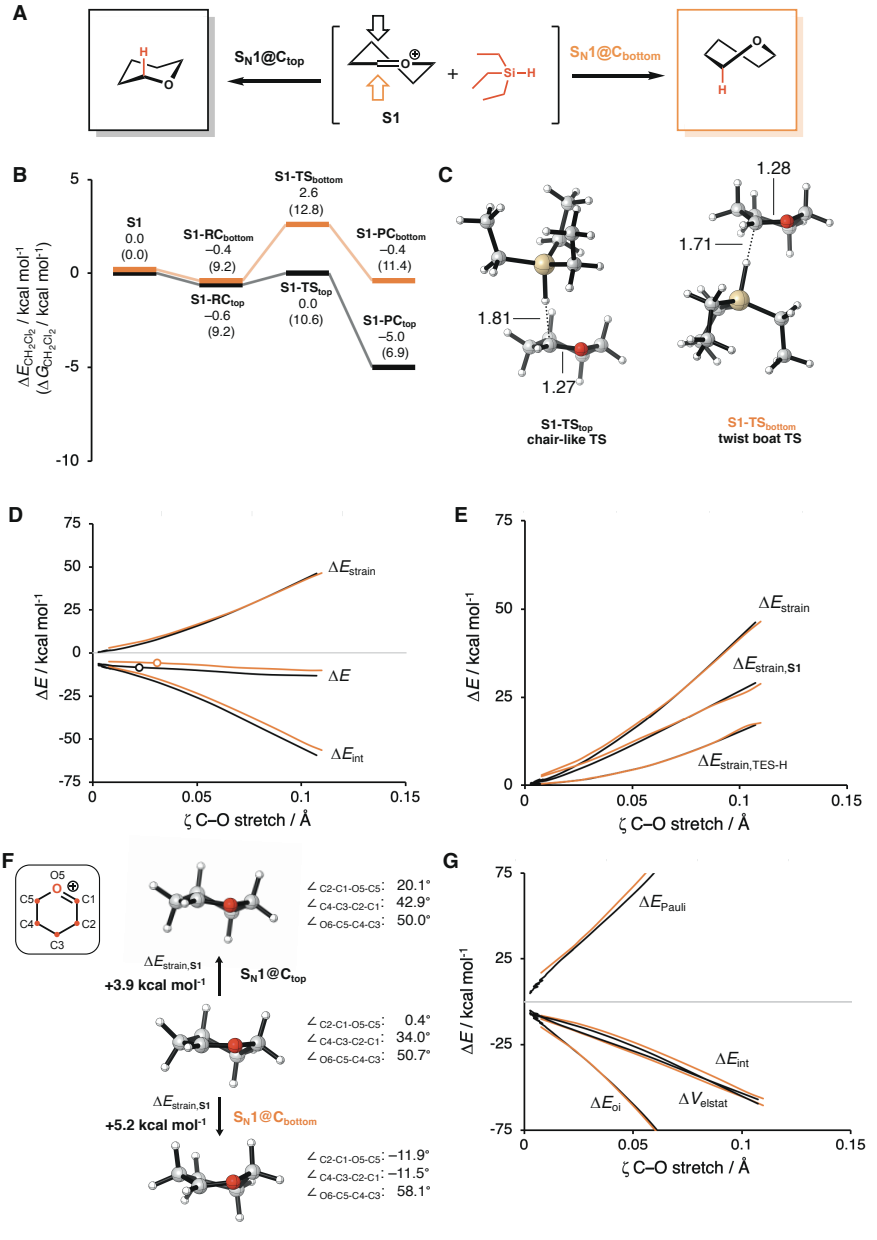
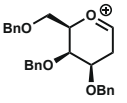


Figure S4. (A) Computationally analyzed triethylsilane addition reactions of model glycosyl cation **S1**; (B) Reaction profiles for the top and bottom face addition reactions computed at PCM(CH_2Cl_2)-B3LYP/6-311G(d,p) and expressed as $\Delta E_{CH_2Cl_2}$ and $\Delta G_{CH_2Cl_2}$ values in kcal mol^{-1}; (C) The transition state structures with key bond lengths (in Å); (D) Activation strain analysis; and (E) Strain decomposition analysis; (F) Deformation of the glycosyl cation upon the attack from the top face and bottom face at consistent geometries with a C–O bond stretch of 0.022 Å; and (G) Energy decomposition analysis of the addition reaction of model glycosyl cation **S1**, where the energy values are projected on the C–O bond stretch; TSs are indicated by dots; Computed in the gas-phase at ZORA-B3LYP/TZ2P//PCM(CH_2Cl_2)-B3LYP/6-311G(d,p).

DFT analysis of 11

Table S2. Computed and experimentally found stereoselectivity for *d*- and *C*-glycosylation reactions on glycosyl cations. The *cis*:*trans* ratio is expressed as the relationship between the substituent on C3-position and the coupled nucleophile; For the computational studies, per-*O*-methylated oxocarbenium ions were used, where the experimental glycosylation used per-*O*-benzylated substrates. All data computed at PCM(CH_2Cl_2)-B3LYP/6-311G(d,p). $\Delta\Delta G^\circ$ is expressed as $\Delta\Delta G^\circ = \Delta G^\circ{}_{^3H_4} - \Delta G^\circ{}_{^4H_3}$. The $\Delta\Delta G^\ddagger_{addition}$ is expressed as $\Delta\Delta G^\ddagger_{addition} = \Delta G^\ddagger_{top} - \Delta G^\ddagger_{bottom}$, and both $\Delta G^\ddagger_{top}$ and $\Delta G^\ddagger_{bottom}$ are relative to the lowest-energy conformer.[42,43]



11

Glycosyl cation	
$\Delta G^\circ{}_{^3H_4}$	0.0
$\Delta G^\circ{}_{^4H_3}$	3.2
$\Delta\Delta G^\circ$	–3.2
$\Delta G^\ddagger_{conf}$	7.0
triethylsilane (TES-d/H) addition	
exp.	**>98:2**
$\Delta G^\ddagger_{top}$	9.9
$\Delta G^\ddagger_{bottom}$	13.4
$\Delta\Delta G^\ddagger_{addition}$	–3.5
comp.	**>98:2**
allyltrimethylsilane (allyl-TMS) addition	
exp.	**>98:2**
$\Delta G^\ddagger_{top}$	10.4
$\Delta G^\ddagger_{bottom}$	12.8
$\Delta\Delta G^\ddagger$	–2.4
comp.	**>98:2**

Strain decomposition analysis of cation 1, 8, 10 and 14

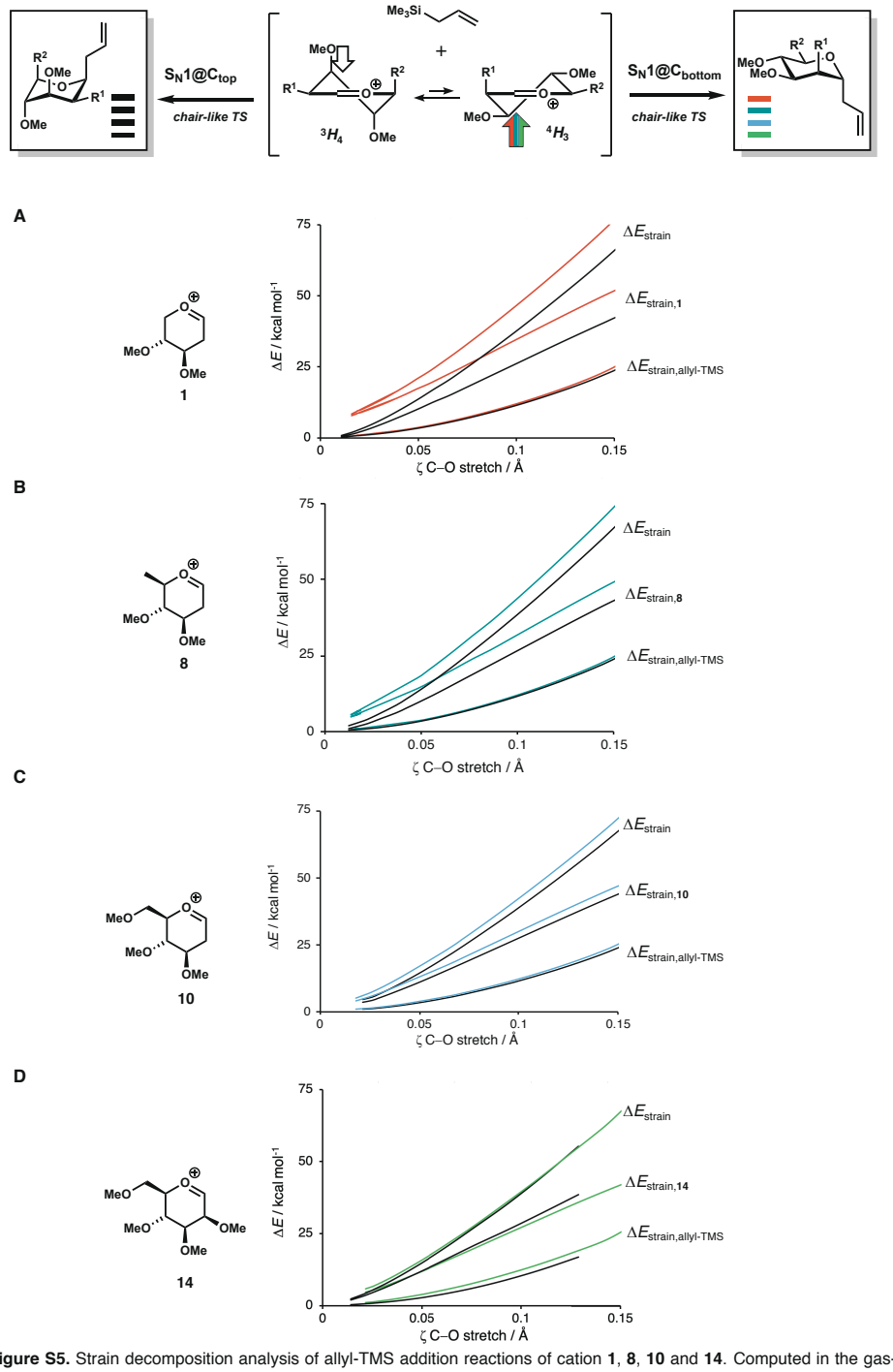


Figure S5. Strain decomposition analysis of allyl-TMS addition reactions of cation **1**, **8**, **10** and **14**. Computed in the gas-phase at ZORA-B3LYP/TZ2P//PCM(CH_2Cl_2)-B3LYP/6-311G(d,p).

Numerical experiment consistent C–O bond stretch and Nuc···C bond distance of 1, 8, 10 and 14

Table S3. Numerical experiment with a consistent C–O bond stretch and Nuc···C bond distance of **1**, **8**, **10** and **14**. Activation strain and energy decomposition analyses (in kcal mol^{-1}) for the allyl-TMS addition reaction at cation **1**, **8**, **10** and **14**. Analyses at consistent geometries with a C–O bond stretch of 0.03 Å and a Nuc···C bond distance of 2.45 Å. Computed at ZORA-B3LYP/TZ2P//PCM(CH_2Cl_2)-B3LYP/6-311G(d,p).

	ΔE^*	ΔE_{strain}	ΔE_{int}	ΔV_{elstat}	ΔE_{Pauli}	ΔE_{oi}
1$_{top\ face}$	–8.6	6.5	–15.1	–19.9	32.4	–27.6
1$_{bottom\ face}$	–4.3	13.5	–17.8	–20.5	32.6	–29.8
8$_{top\ face}$	–5.3	6.6	–12.0	–19.3	34.3	–27.0
8$_{bottom\ face}$	–7.3	8.8	–16.2	–19.5	32.6	–29.3
10$_{top\ face}$	–5.5	6.6	–12.1	–21.0	36.1	–27.2
10$_{bottom\ face}$	–6.1	8.9	–15.0	–20.0	32.5	–27.6
14$_{top\ face}$	–6.7	7.3	–14.1	–22.5	38.8	–30.4
14$_{bottom\ face}$	–6.9	8.8	–15.6	–19.9	32.5	–28.2

Numerical experiment consistent C–O bond stretch and Nuc···C bond distance of 1

Table S4. Numerical experiment with a consistent C–O bond stretch and Nuc···C bond distance of **10**. Activation strain and energy decomposition analyses (in kcal mol^{-1}) for allyl-TMS and triethylsilane addition reactions at cation **10**. Analyses at consistent geometries with a C–O bond stretch of 0.03 Å and a Nuc···C bond stretch of 0.95 Å (measured from the product). Computed at ZORA-B3LYP/TZ2P//PCM(CH_2Cl_2)-B3LYP/6-311G(d,p). All relative energies ($\Delta\Delta E$) are reported with respect to the conversion of $^4H_3 \rightarrow {}^3H_4$, (*e.g.*, $\Delta\Delta E$ is expressed as $\Delta\Delta E = \Delta E_{^3H_4} - \Delta E_{^4H_3}$).

	$\Delta\Delta E^*$	$\Delta\Delta E_{strain}$	$\Delta\Delta E_{int}$	$\Delta\Delta V_{elstat}$	$\Delta\Delta E_{Pauli}$	$\Delta\Delta E_{oi}$
10$_{allyl\text{-}TMS}$	0.6	–2.3	2.9	–1.1	3.6	0.3
10$_{TESH}$	0.2	–2.6	2.8	0.2	1.8	0.8

Orbital analysis: Pauli repulsion

Cation 10

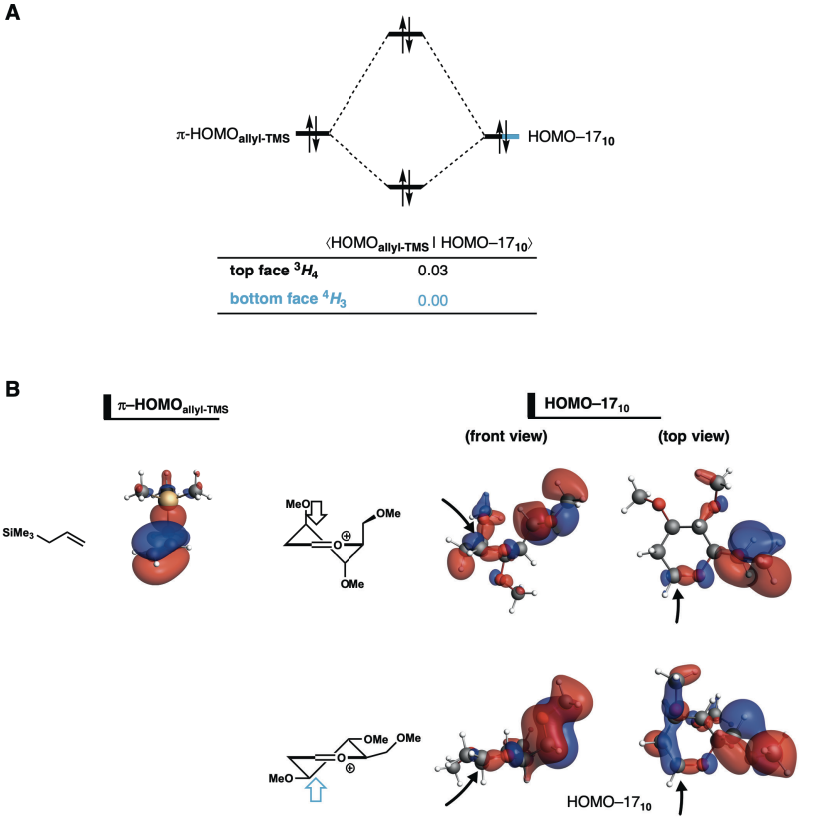
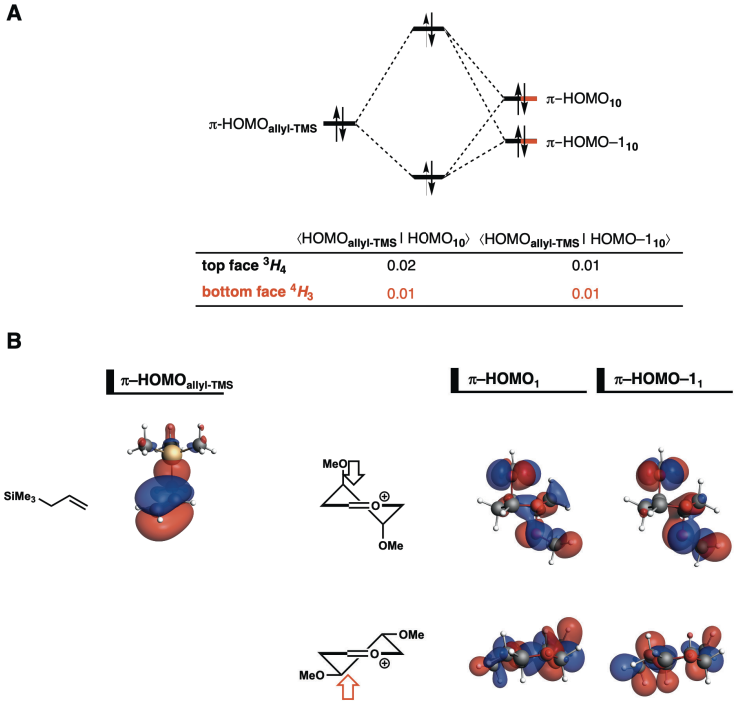


Figure S6. (A) Molecular orbital diagram of the most important occupied–occupied orbital overlap of the addition reaction of **10**; and (B) key occupied orbitals (isovalue = 0.03 Bohr$^{-3/2}$) computed at consistent geometries with a C–O bond stretch of 0.03 Å and a Nuc···C bond distance of 2.45 Å. Computed in the gas-phase at ZORA-B3LYP/TZ2P//PCM(CH_2Cl_2)-B3LYP/6-311G(d,p).

Cation 1 (focus on π–HOMOs on the substituents of the cation)

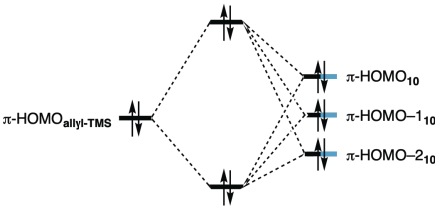


	⟨HOMO$_{allyl-TMS}$ I HOMO$_{10}$⟩	⟨HOMO$_{allyl-TMS}$ I HOMO–1$_{10}$⟩
top face $^3H_4$	0.02	0.01
bottom face $^4H_3$	0.01	0.01

Figure S7. (A) Molecular orbital diagram of the occupied–occupied orbital overlap of the addition reaction of **1**; and (B) occupied orbitals (isovalue = 0.03 Bohr$^{-3/2}$) computed at consistent geometries with a C–O bond stretch of 0.03 Å and a Nuc···C bond distance of 2.45 Å. Computed in the gas-phase at ZORA-B3LYP/TZ2P//PCM(CH_2Cl_2)-B3LYP/6-311G(d,p).

Cation 10 (focus on π–HOMOs on the substituents of the cation)

A



	⟨HOMO$_{allyl-TMS}$ I HOMO$_{10}$⟩	⟨HOMO$_{allyl-TMS}$ I HOMO–1$_{10}$⟩	⟨HOMO$_{allyl-TMS}$ I HOMO–2$_{10}$⟩
top face $^3H_4$	0.01	0.01	0.00
bottom face $^4H_3$	0.01	0.00	0.00

B

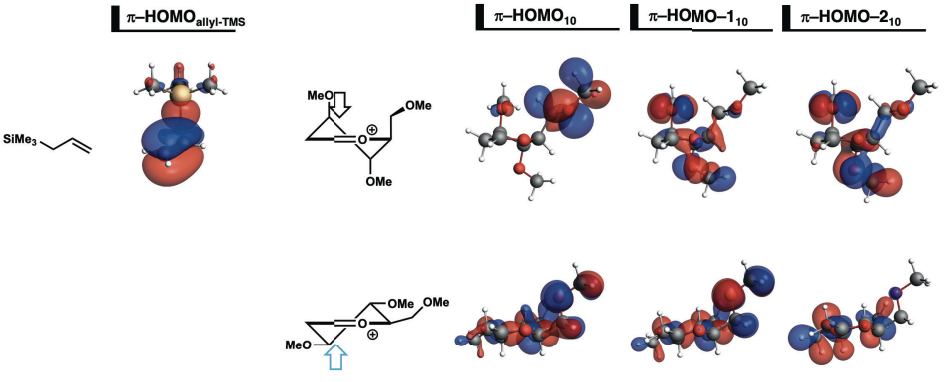


Figure S8. (A) Molecular orbital diagram of the occupied–occupied orbital overlap of the addition reaction of **10**; and (B) occupied orbitals (isovalue = 0.03 Bohr$^{-3/2}$) computed at consistent geometries with a C–O bond stretch of 0.03 Å and a Nuc···C bond distance of 2.45 Å. Computed in the gas-phase at ZORA-B3LYP/TZ2P//PCM(CH_2Cl_2)-B3LYP/6-311G(d,p).

ASM and EDA analysis of cation 1 with TES-H

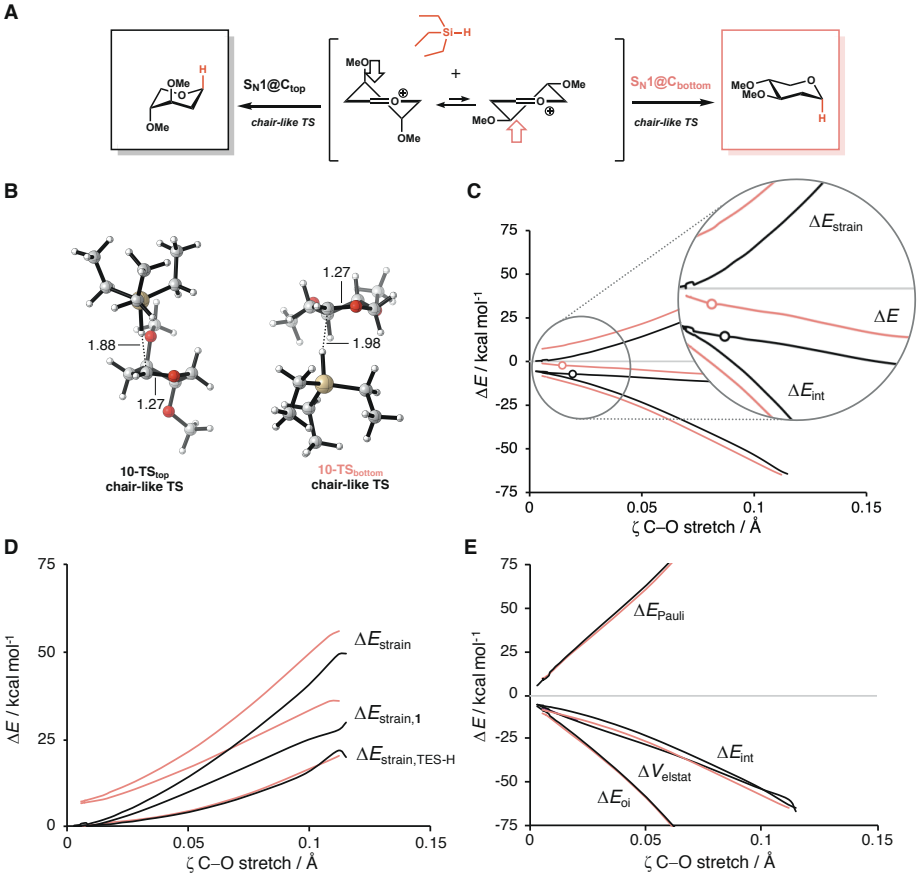


Figure S9. (A) Computationally analyzed TES-H addition reactions of glycosyl cation **1**; (B) The transition state structures with key bond lengths (in Å); (C) Activation strain analysis; (D) Strain decomposition analysis and (E) Energy decomposition analysis of the addition reaction of **1**, where the energy values are projected on the C–O stretch; TSs are indicated by dots; Computed in the gas-phase at ZORA-B3LYP/TZ2P//PCM(CH_2Cl_2)-B3LYP/6-311G(d,p).

ASM and EDA analysis of cation 10 with TES-H

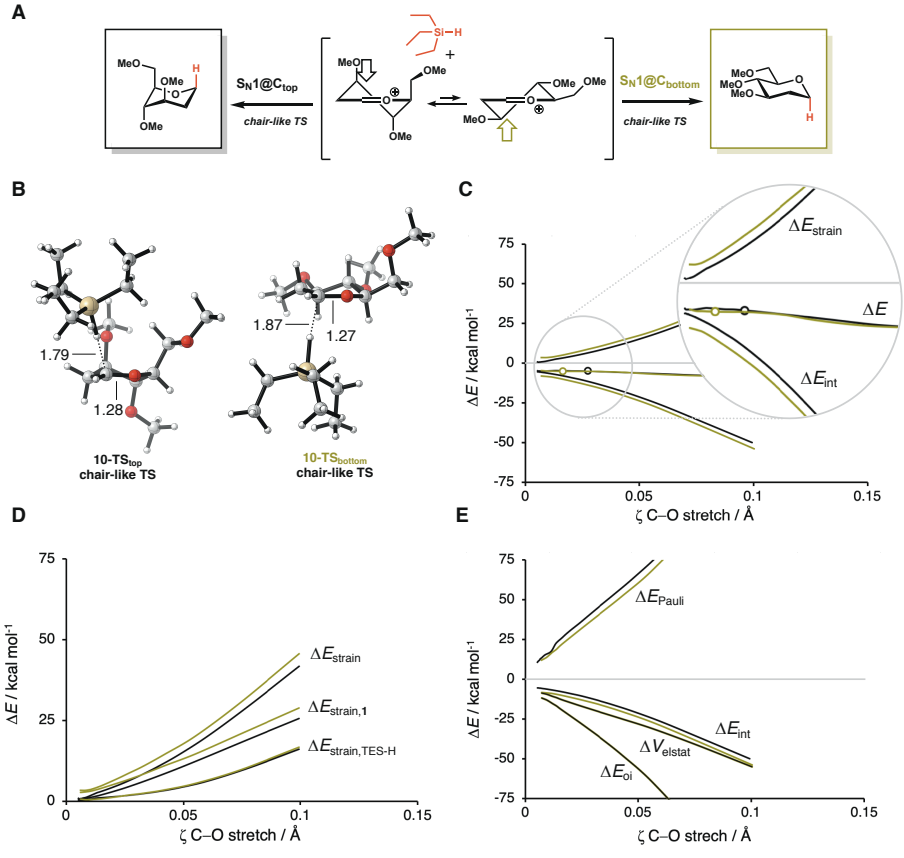


Figure S10. (A) Computationally analyzed TES-H addition reactions of glycosyl cation **10**; (B) The transition state structures with key bond lengths (in Å); (C) Activation strain analysis; (D) Strain decomposition analysis and (E) Energy decomposition analysis of the addition reaction of **10**, where the energy values are projected on the C–O stretch; TSs are indicated by dots; Computed in the gas-phase at ZORA-B3LYP/TZ2P//PCM(CH_2Cl_2)-B3LYP/6-311G(d,p).

Homolytic cleavage (spin-unrestricted fragmentation): ASM and EDA analysis of S2

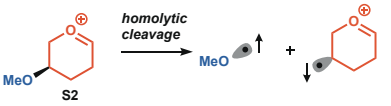
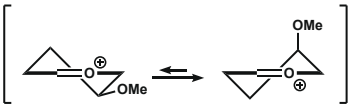


Figure S11. Activation strain and energy decomposition analysis of cation **S2**. All energies are computed at ZORA-B3LYP/TZ2P//PCM(CH_2Cl_2)-B3LYP/6-311G(d,p). All energies are reported with respect to the $^3H_4 \rightarrow {}^4H_3$ conversion and are expressed in kcal mol^{-1}.

$$\Delta\Delta E = \Delta E^{4H3} - \Delta E^{3H4} \qquad \text{(Eq. S7)}$$

Table S5. Activation strain and energy decomposition analysis of cation **S2**. All energies are computed at ZORA-B3LYP/TZ2P//PCM(CH_2Cl_2)-B3LYP/6-311G(d,p). All energies are reported with respect to the $^3H_4 \rightarrow {}^4H_3$ conversion and are expressed in kcal mol^{-1}.



	Pref. geom.	$\Delta\Delta E$	$\Delta\Delta E^{cation}_{strain}$	$\Delta\Delta E^{subs}_{strain}$	$\Delta\Delta E_{int}$	$\Delta\Delta V_{elstat}$	$\Delta\Delta E_{Pauli}$	$\Delta\Delta E_{oi}$
S2	$^4H_3$	–14.2	–8.4	–0.5	–5.3	–31.6	39.7	–13.4

Organic synthesis

General experimental procedures

All chemicals (Acros, Fluka, Merck, and Sigma-Aldrich) were used as received unless stated otherwise. Dichloromethane was stored over activated 4 Å molecular sieves (beads, 8-12 mesh, Sigma-Aldrich). Before use traces of water present in the donor, diphenyl sulfoxide (Ph_2SO) and tri-*tert*-butylpyrimidine (TTBP) were removed by co-evaporation with dry toluene. The acceptor, allyltrimethylsilane, was stored in stock solutions (DCM, 0.5 M) over activated 4 Å molecular sieves. Trifluoromethanesulfonic anhydride (Tf_2O) was distilled over P_2O_5 and stored at –20 °C under a nitrogen atmosphere. Overnight temperature control was achieved by an FT902 Immersion Cooler (Julabo). Column chromatography was performed on silica gel 60 Å (0.04 – 0.063 mm, Screening Devices B.V.). Size exclusion chromatography was carried out on Sephadex^{TM} (LH-20, GE Healthcare Life Sciences) by isocratic elution with DCM:MeOH (1:1, v:v). TLC-analysis was conducted on TLC Silica gel 60 (Kieselgel 60 F_{254}, Merck) with UV detection by (254 nm) and by spraying with 20% sulfuric acid in ethanol followed by charring at ± 150 °C or by spraying with a solution of $(NH_4)_6Mo_7O_{24}{\cdot}H_2O$ (25 g/l) and $(NH_4)_4Ce(SO_4)_4{\cdot}2H_2O$ (10 g/l) in 10% sulfuric acid in water followed by charring at ± 260 °C. High-resolution mass spectra were recorded on a Thermo Finnigan LTQ Orbitrap mass spectrometer equipped with an electrospray ion source in positive mode (source voltage 3.5 kV, sheath gas flow 10, capillary temperature 275 °C) with resolution R=60.000 at m/z=400 (mass range = 150-4000). ^{1}H, ^{2}H and ^{13}C NMR spectra were recorded on a Bruker AV-400 NMR instrument (400, 61 and 101 MHz respectively), a Bruker AV-500 NMR instrument (500, 75 and 126 MHz respectively), or a Bruker AV-600 NMR instrument (600, 92 and 150 MHz respectively). For samples measured in $CDCl_3$ chemical shifts (δ) are given in ppm relative to tetramethylsilane as an internal standard or the residual signal of the deuterated solvent. Coupling constants (J) are given in Hz. To get better resolution of signals with small coupling constants or overlapping signals a gaussian window function (LB = ± –1 and GB = ± 0.5) was used on the ^{1}H NMR spectrum. All given ^{13}C APT spectra are proton decoupled. NMR peak assignment was made using COSY, HSQC. If necessary additional NOESY, HMBC and HMBC-GATED experiments were used to elucidate the structure. The anomeric product ratios were based on the integration of ^{1}H NMR. If the stereochemistry of the coupled product could not be confirmed a deprotection step was performed to verify the stereochemistry. IR spectra were recorded on a Shimadzu FTIR-8300 IR spectrometer with a resolution of 4 cm^{-1} and are reported in cm^{-1}. Specific rotations were measured on an MCP 100 Anton Paar polarimeter in $CHCl_3$ (10 mg/mL) at 589 nm unless stated otherwise.

General procedure I: pre-activation Tf_2O/Ph_2SO based *C*-glycosylation

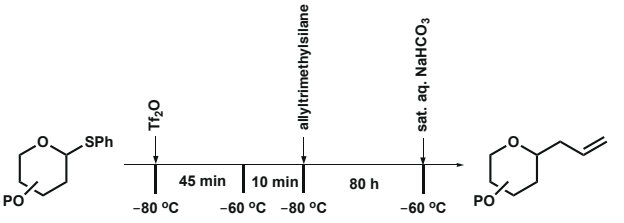
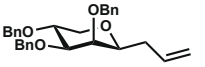
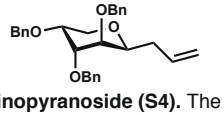


Figure S11. Schematic representation of the reaction procedure during pre-activation Ph_2SO/Tf_2O mediated glycosylation.[18]

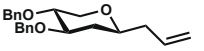
A solution of the donor (100 µmol), Ph_2SO (26 mg, 130 µmol, 1.3 eq.) and TTBP (62 mg, 250 µmol, 2.5 eq.) in DCM (2 mL, 0.05 M) was stirred over activated 3 Å molecular sieves (rods, size 1/16 in., Sigma-Aldrich) for 30 min under an atmosphere of N_2. The solution was cooled to −80 °C and Tf_2O (22 µl, 130 µmol, 1.3 eq.) was slowly added to the reaction mixture. The reaction mixture was allowed to warm to −60 °C in approximately 45 min, followed by cooling to −80 °C and the addition of the acceptor (200 µmol, 2 eq.) in DCM (0.4 mL, 0.5 M). The reaction was allowed to warm up to −60 °C and stirred for an additional 80 h at this temperature to ensure reaction completion. The reaction was quenched with sat. aq. $NaHCO_3$ at −60 °C and diluted with DCM (5 mL). The resulting solution was washed with H_2O and brine, dried over $MgSO_4$, filtered and concentrated under reduced pressure. Purification by column chromatography yielded the corresponding *C*-coupled glycoside.



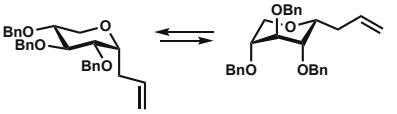
Allyl 2,3,4-tri-*O*-benzyl-1-deoxy-D-lyxopyranoside (S3). The title compound was prepared according to general procedure I. Column chromatography (95:5 → 80:20, pentane:Et_2O) yielded the title compound (36 mg, 81 µmol, 81%, colorless oil, 1,2-*cis*:1,2-*trans*; >98:2). Spectroscopic data was in accordance with literature.[72] TLC: R_f 0.30 (pentane:Et_2O, 9:1, v:v); $[\alpha]_D^{25}$ 5.2°; IR (thin film, cm^{-1}): 695, 1091, 1361, 1450, 1480, 2855, 3012; ^1H NMR (500 MHz, Chloroform-*d,* HH-COSY, HSQC, HMBC, HH-NOESY): δ 7.85 – 6.84 (m, 15H, CH_{arom}), 5.77 – 5.55 (m, 1H, C*H* allyl), 5.05 – 4.95 (m, 3H, CH_2 allyl, C*H*H Bn), 4.89 – 4.73 (m, 3H, C*H*H Bn, C*H*H Bn, CH*H* Bn), 4.65 (m, 2H, CH*H* Bn, CH*H* Bn), 4.14 – 3.99 (m, 2H, H-4, H-5_{eq}), 3.76 (dd, *J* = 2.9, 1.1 Hz, 1H, H-2), 3.53 (dd, *J* = 8.8, 2.8 Hz, 1H, H-3), 3.26 (ddd, *J* = 7.4, 6.3, 1.1 Hz, 1H, H-1), 3.15 (dd, *J* = 12.8, 11.9 Hz, 1H, H-5_{ax}), 2.43 (dddt, *J* = 14.0, 7.9, 6.7, 1.4 Hz, 1H, C*H*H allylic), 2.25 – 2.17 (m, 1H, CH*H* allylic); ^{13}C NMR (126 MHz, $CDCl_3$, HSQC): δ 138.8, 138.7, 138.7 ($C_{q\text{-}arom}$), 134.8 (*C*H allyl), 128.9, 128.6, 128.5, 128.5, 128.5, 128.4, 128.1, 127.8, 127.8, 127.7, 127.6 (CH_{arom}), 117.0 (*C*H_2 allyl), 83.7 (C-3), 79.1 (C-1), 75.6 (C-2), 75.4 (C-4), 74.8, 73.7, 73.0 (CH_2 Bn), 68.9 (C-5), 36.9 (*C*H_2 allylic); HRMS: $[M+Na]^+$ calcd for $C_{29}H_{32}NaO_4$ 467.2192, found 467.2190.



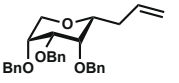
Allyl 2,3,4-tri-*O*-benzyl-1-deoxy-D-arabinopyranoside (S4). The title compound was prepared according to general procedure I. Column chromatography (95:5 → 80:20, pentane:Et_2O) yielded the title compound (30 mg, 68 µmol, 68%, colorless oil, 1,2-*cis*:1,2-*trans*; >98:2). Spectroscopic data was in accordance with literature.[72] TLC: R_f 0.35 (pentane:Et_2O, 9:1, v:v); $[\alpha]_D^{25}$ −7.8°; IR (thin film, cm^{-1}): 1056, 1360, 1451, 1455, 2857, 3015; ^1H NMR (500 MHz, Chloroform-*d,* HH-COSY, HSQC, HMBC, HH-NOESY): δ 7.53 – 7.19 (m, 15H, CH_{arom}), 5.69 (dddd, *J* = 16.9, 10.2, 7.5, 6.5 Hz, 1H, C*H* allyl), 5.09 – 4.94 (m, 2H, CH_2 allyl), 4.75 (d, *J* = 12.2 Hz, 1H, C*H*H Bn), 4.60 – 4.45 (m, 3H, CH*H* Bn, C*H*H Bn, CH*H* Bn), 4.43 (d, *J* = 11.9 Hz, 1H, C*H*H Bn), 4.39 (d, *J* = 11.9 Hz, 1H, CH*H* Bn), 3.90 – 3.79 (m, 3H, H-3, H-4, H-5), 3.76 – 3.69 (m, 1H, H-1), 3.72 (t, *J* = 10.6 Hz, 1H, H-5), 3.34 (dd, *J* = 3.9, 1.5 Hz, 1H, H-2), 2.38 (dddt, *J* = 14.2, 7.9, 6.5, 1.5 Hz, 1H, C*H*H allylic), 2.17 (dddt, *J* = 14.1, 7.6, 6.5, 1.3 Hz, 1H, CH*H* allylic); ^{13}C NMR (126 MHz, $CDCl_3$, HSQC): δ 138.8, 138.5, 138.1 ($C_{q\text{-}arom}$), 135.1 (*C*H allyl), 128.5, 128.5, 128.5, 128.3, 128.2, 128.1, 127.9, 127.8, 127.8, 127.8 (CH_{arom}), 117.1 (*C*H_2 allyl), 76.4 (C-2), 74.4 (C-1), 73.2 (CH_2 Bn), 73.1 (C-4), 72.9 (CH_2 Bn), 72.6 (C-3), 71.5 (CH_2 Bn), 64.7 (C-5), 35.3 (*C*H_2 allylic); HRMS: $[M+Na]^+$ calcd for $C_{29}H_{32}NaO_4$ 467.2192, found 467.2196.



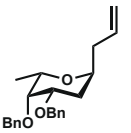
Allyl 3,4-di-*O*-benzyl-1,2-di-deoxy-D-xylopyranoside (S5). The title compound was prepared according to general procedure I. Column chromatography (95:5 → 80:20, pentane:Et_2O) yielded the title compound (20 mg, 59 µmol, 59%, colorless oil, 1,3-*cis*:1,3-*trans*; >98:2). TLC: R_f 0.37 (pentane:Et_2O, 9:1, v:v); $[\alpha]_D^{25}$ 2.2°; IR (thin film, cm^{-1}): 691, 1109, 1387, 1443, 1455, 2876; ^1H NMR (500 MHz, Chloroform-*d,* HH-COSY, HSQC, HMBC, HH-NOESY): δ 7.36 – 7.18 (m, 10H, CH_{arom}), 5.79 (ddt, *J* = 17.2, 10.2, 7.0 Hz, 1H, C*H* allyl), 5.15 – 4.99 (m, 2H, CH_2 allyl), 4.79 (d, *J* = 11.7 Hz, 1H, *C*HH Bn), 4.71 (s, 2H, CH_2 Bn), 4.66 (d, *J* = 11.7 Hz, 1H, CH*H* Bn), 4.02 (dd, *J* = 11.3, 5.1 Hz, 1H, H-5_{eq}), 3.60 – 3.43 (m, 2H, H-3, H-4), 3.42 – 3.26 (m, 1H, H-1), 3.14 (dd, *J* = 11.3, 10.1 Hz, 1H, H-5_{ax}), 2.36 – 2.25 (m, 1H, C*H*H allylic), 2.25 – 2.15 (m, 1H, CH*H* allylic), 2.11 (ddd, *J* = 13.1, 4.9, 2.0 Hz, 1H, H-2_{eq}), 1.36 (dt, *J* = 13.0, 11.2 Hz, 1H, H-2_{ax}); ^{13}C NMR (126 MHz, $CDCl_3$, HSQC): δ 139.0, 138.5 ($C_{q\text{-}arom}$), 135.5 (*C*H allyl), 128.5, 128.5, 127.9, 127.8, 127.7, 127.7 (CH_{arom}), 117.4 (*C*H_2 allyl), 79.9 (C-3), 78.7 (C-4), 75.9 (C-1), 73.4, 72.0 (CH_2 Bn), 68.5 (C-5), 39.7 (*C*H_2 allylic), 37.4 (C-2); HRMS: $[M+Na]^+$ calcd for $C_{22}H_{26}NaO_3$ 361.1774, found 361.1770.



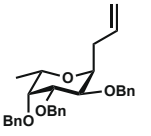
Allyl 2,3,4-tri-*O*-benzyl-1-deoxy-D-xylopyranoside (S6). The title compound was prepared according to general procedure I. Column chromatography (95:5 → 80:20, pentane:Et_2O) yielded the title compound (32 mg, 72 µmol, 72%, colorless oil, 1,2-*cis*:1,2-*trans*; >98:2). Spectroscopic data was in accordance with literature.[72] TLC: R_f 0.25 (pentane:Et_2O, 9:1, v:v); $[\alpha]_D^{25}$ 8.9°; IR (thin film, cm^{-1}): 1101, 1360, 1451, 1489, 2869, 3001; ^1H NMR (500 MHz, Chloroform-*d,* HH-COSY, HSQC, HMBC, HH-NOESY): δ 7.38 – 7.26 (m, 15H, CH_{arom}), 5.77 (ddt, *J* = 17.1, 10.2, 7.0 Hz, 1H, C*H* allyl), 5.13 – 5.01 (m, 2H, CH_2 allyl), 4.65 (d, *J* = 11.8 Hz, 1H, C*H*H Bn), 4.62 – 4.56 (m, 4H, C*H*H Bn, CH*H* Bn, C*H*H Bn, CH*H* Bn), 4.51 (d, *J* = 11.8 Hz, 1H, CH*H* Bn), 3.79 (ddd, *J* = 7.2, 5.2, 3.4 Hz, 1H, H-1), 3.77 – 3.70 (m, 2H, H-3, H-5), 3.46 – 3.37 (m, 1H, H-4) 3.42 (dd, *J* = 5.3, 3.7 Hz, 1H, H-2), 2.59 – 2.49 (m, 1H, C*H*H allylic), 2.36 (dddd, *J* = 13.4, 8.3, 4.1, 2.6 Hz, 1H, CH*H* allylic); ^{13}C NMR (126 MHz, $CDCl_3$, HSQC): 138.5, 138.4 ($C_{q\text{-}arom}$), 135.1 (*C*H allyl), 128.6, 128.5, 128.5, 128.3, 128.0, 127.9, 127.9, 127.8 (CH_{arom}), 117.1 (*C*H_2 allyl), 76.5, (C-2) 75.3 (C-1), 75.0 (C-3), 74.9 (C-4), 73.6, 72.8, 72.3 (CH_2 Bn), 64.7 (C-5), 33.1 (*C*H_2 allylic); HRMS: $[M+Na]^+$ calcd for $C_{29}H_{32}NaO_4$ 467.2192, found 467.2189.



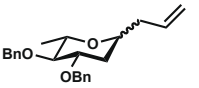
Allyl 2,3,4-tri-*O*-benzyl-1-deoxy-D-ribopyranoside (S7). The title compound was prepared according to general procedure I. Column chromatography (95:5 → 80:20, pentane:Et_2O) yielded the title compound (28 mg, 63 µmol, 63%, colorless oil, 1,2-*cis*:1,2-*trans*; >98:2). Spectroscopic data was in accordance with literature.[72] TLC: R_f 0.12 (pentane:Et_2O, 9:1, v:v); $[\alpha]_D^{25}$ 4.4°; IR (thin film, cm^{-1}): 1098, 1369, 1420, 1476, 2850, 3062; ^1H NMR (500 MHz, Chloroform-*d,* HH-COSY, HSQC, HMBC, HH-NOESY): δ 7.44 – 7.22 (m, 15H, CH_{arom}), 5.77 (ddt, *J* = 17.2, 10.1, 7.1 Hz, 1H, C*H* allyl), 5.12 – 5.00 (m, 2H, CH_2 allyl), 4.94 (d, *J* = 11.8 Hz, 1H, C*H*H Bn), 4.80 (d, *J* = 12.5 Hz, 1H, C*H*H Bn), 4.73 (d, *J* = 11.8 Hz, 1H, CH*H* Bn), 4.69 – 4.57 (m, 3H, CH*H* Bn, C*H*H Bn, CH*H* Bn), 4.10 (dd, *J* = 12.2, 4.3 Hz, 1H, H-5), 3.91 – 3.67 (m, 3H, H-2, H-3, H-4), 3.46 (bs, 1H, H-1), 3.43 (dd, *J* = 12.2, 2.5 Hz, 1H, H-5), 2.73 (dt, *J* = 15.3, 7.8 Hz, 1H, C*H*H allylic), 2.41 (dddd, *J* = 13.4, 7.0, 4.0, 1.3 Hz, 1H, CH*H* allylic); ^{13}C NMR (126 MHz, $CDCl_3$, HSQC): δ 139.0, 138.8, 138.6 ($C_{q\text{-}arom}$), 135.6 (*C*H allyl), 128.5, 128.4, 128.3, 128.2, 128.0, 127.6, 127.5, 127.5, 127.4 (CH_{arom}), 117.0 (*C*H_2 allyl), 78.8 (C-3), 78.2 (C-1), 74.6 (C-2), 73.2 (CH_2 Bn), 73.1 (C-4), 71.9, 71.6 (CH_2 Bn), 66.0 (C-5), 34.6 (*C*H_2 allyl); HRMS: $[M+Na]^+$ calcd for $C_{29}H_{32}NaO_4$ 467.2192, found 467.2191.



Allyl 2,3,4-tri-*O*-benzyl-1,2-dideoxy-D-fucopyranoside (S8). The title compound was prepared according to general procedure I. Column chromatography (95:5 → 80:20, pentane:Et_2O) yielded the title compound (34 mg, 96 µmol, 96%, colorless oil, 1,3-*cis*:1,3-*trans*; <2:98). TLC: R_f 0.30 (pentane:Et_2O, 9:1, v:v); $[\alpha]_D^{25}$ –32.9°; IR (thin film, cm^{-1}): 1100, 1390, 1410, 1490, 2860; ^{1}H NMR (500 MHz, Chloroform-*d,* HH-COSY, HSQC, HMBC, HH-NOESY): δ 7.53 – 7.03 (m, 10H), 5.83 – 5.71 (m, 1H, C*H* allyl), 5.08 – 4.99 (m, 2H, CH_2 allyl), 4.77 (d, *J* = 12.0 Hz, 1H, C*H*H Bn), 4.70 – 4.58 (m, 3H, CH*H* Bn, C*H*H Bn, CH*H* Bn), 4.06 (qd, *J* = 6.7, 4.1 Hz, 1H, H-1), 3.91 (qd, *J* = 6.7, 3.6 Hz, 1H, H-5), 3.85 (dt, *J* = 7.9, 3.2 Hz, 1H, H-3), 3.57 (t, *J* = 3.3 Hz, 1H, H-4), 2.37 – 2.28 (m, 1H, C*H*H allylic), 2.22 – 2.12 (m, 1H, CH*H* allylic), 2.08 (ddd, *J* = 13.3, 8.0, 4.1 Hz, 1H, H-2_{ax}), 1.56 (ddd, *J* = 13.3, 6.6, 3.8 Hz, 1H, H-2_{eq}), 1.33 (d, *J* = 6.6 Hz, 3H, CH_3); ^{13}C NMR (126 MHz, $CDCl_3$, HSQC): δ 139.0, 138.9 ($C_{q\text{-}arom}$), 134.5 (*C*H allyl), 128.5, 128.4, 128.0, 127.6, 127.6, 127.4 (CH_{arom}), 116.9 (*C*H_2 allyl), 76.6 (C-4), 73.9 (C-3), 72.6, 71.3 (CH_2 Bn), 69.5 (C-5), 68.0 (C-1), 38.0 (*C*H_2 allylic), 31.7 (C-2), 16.6 (CH_3); HRMS: $[M+Na]^+$ calcd for $C_{23}H_{28}NO_3$ 375.1930, found 375.1926.

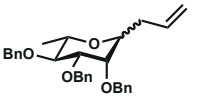


Allyl 2,3,4-tri-*O*-benzyl-1-deoxy-D-fucosepyranoside (S9). The title compound was prepared according to general procedure I. Column chromatography (95:5 → 80:20, pentane:Et_2O) yielded the title compound (35 mg, 76 µmol, 76%, colorless oil, 1,2-*cis*:1,2-*trans*; >98:2). Spectroscopic data was in accordance with literature.[73] TLC: R_f 0.43 (pentane:Et_2O, 9:1, v:v); $[\alpha]_D^{25}$ –36.7°; IR (thin film, cm^{-1}): 699, 1160, 1350, 1440, 1431, 2880, 2910; ^{1}H NMR (500 MHz, Chloroform-*d,* HH-COSY, HSQC, HMBC, HH-NOESY): δ 8.06 – 6.84 (m, 15H, CH_{arom}), 5.76 (ddt, *J* = 17.1, 10.2, 6.9 Hz, 1H, C*H* allyl), 5.14 – 4.93 (m, 2H, CH_2 allyl), 4.80 – 4.53 (m, 5H, C*H*H Bn, CH*H* Bn, C*H*H Bn, CH*H* Bn, C*H*H Bn), 4.52 (d, *J* = 11.8 Hz, 1H, CH*H* Bn), 4.06 (ddd, *J* = 8.5, 5.2, 2.4 Hz, 1H, H-1), 3.95 (dd, *J* = 6.7, 3.8 Hz, 1H, H-5), 3.82 – 3.70 (m, 3H, H-2, H-3, H-4), 2.40 (dddt, *J* = 14.7, 9.4, 6.8, 1.4 Hz, 1H, C*H*H allylic), 2.31 (dddd, *J* = 13.4, 6.9, 4.1, 1.4 Hz, 1H, CH*H* allylic), 1.29 (d, *J* = 6.7 Hz, 3H, CH_3); ^{13}C NMR (126 MHz, $CDCl_3$, HSQC): δ 139.0, 138.7, 138.5 ($C_{q\text{-}arom}$), 135.5 (*C*H allyl), 128.5, 128.4, 128.3, 128.1, 127.9, 127.7, 127.7, 127.7, 127.6 (CH_{arom}), 117.9 (*C*H_2 allyl), 76.9 (C-3), 76.7 (C-4), 76.0 (C-2), 73.2, 73.1, 73.1(CH_2 Bn), 70.3, (C-1), 68.8 (C-5), 31.2 (*C*H_2 allylic), 14.5 (CH_3); HRMS: $[M+Na]^+$ calcd for $C_{30}H_{34}NaO_4$ 481.2349, found 481.2347.

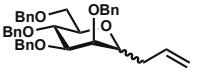


Allyl 2,3,4-tri-*O*-benzyl-1,2-dideoxy-D-rhamnopyranoside (S10). The title compound was prepared according to general procedure I. Column chromatography (95:5 → 80:20, pentane:Et_2O) yielded the title compound (25 mg, 71 µmol, 71%, colorless oil, 1,3-*cis*:1,3-*trans*; 9:91). TLC: R_f 0.32 (1,3-*trans*) and 0.40 (1,3-*cis*) (pentane:Et_2O, 9:1, v:v); IR (thin film, cm^{-1}): 1101, 1384, 1430, 1470, 2841; data of the *trans*-anomer: ^{1}H NMR (500 MHz, Chloroform-*d,* HH-COSY, HSQC, HMBC, HH-NOESY): δ 7.53 – 7.10 (m, 10H, CH_{arom}), 5.75 (ddt, *J* = 16.0, 11.1, 7.0 Hz, 1H, C*H* allyl), 5.12 – 4.99 (m, 2H, CH_2 allyl), 4.86 (d, *J* = 11.1 Hz, 1H, C*H*H Bn), 4.73 – 4.55 (m, 3H, CH*H* Bn, C*H*H Bn, CH*H* Bn), 3.99 (tt, *J* = 8.1, 4.4 Hz, 1H, H-1), 3.77 (ddd, *J* = 9.8, 7.5, 4.5 Hz, 1H, H-3), 3.69 (dq, *J* = 7.8, 6.3 Hz, 1H, H-5), 3.13 (t, *J* = 7.7 Hz, 1H, H-4), 2.45 (dddt, *J* = 14.4, 8.1, 6.7, 1.4 Hz, 1H, C*H*H allylic), 2.21 (dtt, *J* = 14.2, 7.1, 1.2 Hz, 1H, CH*H* allylic), 2.01 (ddd, *J* = 13.3, 4.6, 3.5 Hz, 1H, H-2_{eq}), 1.75 (ddd, *J* = 13.3, 9.9, 5.2 Hz, 1H, H-2_{ax}), 1.29 (d, *J* = 6.2 Hz, 3H, CH_3); ^{13}C NMR (126 MHz, $CDCl_3$, HSQC): δ 138.7, 138.6 ($C_{q\text{-}arom}$), 134.9 (*C*H allyl), 128.5, 128.5, 128.1, 127.8, 127.8, 127.8 (CH_{arom}), 117.1 (*C*H_2 allyl), 83.0 (C-4), 76.8 (C-3), 74.7, 71.5 (CH_2 Bn), 70.6 (C-1), 69.6 (C-5), 36.8 (*C*H_2 allylic), 33.0 (C-2), 18.4 (CH_3); diagnostic signals of the *cis*-anomer: ^{1}H NMR (500 MHz, Chloroform-*d,* HH-COSY, HSQC, HMBC, HH-NOESY): δ 4.95 (d, *J* = 10.9 Hz, 1H, C*H*H Bn), 4.70 (d, *J* = 11.6 Hz, 2H, C*H*H Bn), 3.42 – 3.34 (m, 1H, H-1), 3.35 – 3.28 (m, 1H, H-3), 3.09 (t, *J* = 8.9 Hz, 1H, H-4), 2.40 – 2.25 (m,

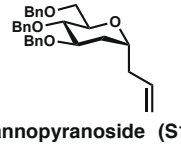
1H, C*H*H allylic); ^{13}C NMR (126 MHz, $CDCl_3$, HSQC): δ 134.6 (*C*H allyl), 117.2 (*C*H_2 allyl), 84.5 (C-4), 75.4 (C-1), 75.4 (C-3), 74.8 (CH_2 Bn); HRMS: $[M+Na]^+$ calcd for $C_{23}H_{28}NO_3$ 375.1930, found 375.1932.



Allyl 2,3,4-tri-*O*-benzyl-1-deoxy-D-rhamnopyranoside (S11). The title compound was prepared according to general procedure I. Column chromatography (95:5 → 80:20, pentane:Et_2O) yielded the title compound (38 mg, 83 µmol, 83%, colorless oil, 1,2-*cis*:1,2-*trans*; 23:77). TLC: R_f 0.34 (1,2-*trans*) and 0.46 (1,2-*cis*) (pentane:Et_2O, 9:1, v:v); IR (thin film, cm^{-1}): 670, 1170, 1350, 1440, 1483, 2842, 2901; data of the *trans*-anomer: ^{1}H NMR (500 MHz, Chloroform-*d,* HH-COSY, HSQC, HMBC, HH-NOESY): δ 7.48 – 7.13 (m, 15H, CH_{arom}), 5.77 – 5.58 (m, 1H, C*H* allyl), 5.05 – 4.91 (m, 2H, C*H*$_2$ allyl), 4.84 (d, *J* = 11.1 Hz, 1H, C*H*H Bn), 4.81 – 4.55 (m, 5H, CH*H* Bn, C*H*H Bn, CH*H* Bn, C*H*H Bn, CH*H* Bn), 4.01 (ddd, *J* = 8.2, 6.6, 3.4 Hz, 1H, H-1), 3.74 (dd, *J* = 7.9, 3.1 Hz, 1H, H-3), 3.67 (dd, *J* = 7.7, 6.1 Hz, 1H, H-5), 3.66 – 3.59 (m, 1H, H-2), 3.58 (t, *J* = 7.8 Hz, 1H, H-4), 2.34 (tdd, *J* = 8.2, 6.5, 1.4 Hz, 1H, C*H*H allylic), 2.23 (dqd, *J* = 14.2, 6.9, 1.6 Hz, 1H, CH*H* allylic), 1.33 (d, *J* = 6.2 Hz, 3H, CH_3); ^{13}C NMR (126 MHz, $CDCl_3$, HSQC): δ 138.9, 138.6, 138.4 ($C_{q\text{-}arom}$), 134.4 (*C*H allyl), 128.6, 128.6, 128.5, 128.5, 128.2, 128.2, 128.0, 127.9, 127.8, 127.8, 127.7, 127.6 (CH_{arom}), 117.9 (*C*H_2 allyl), 80.3 (C-4), 78.1 (C-3), 75.3 (C-2), 74.8 (CH_2 Bn), 73.2 (C-1), 72.1, 71.8 (CH_2 Bn), 69.8 (C-5), 34.1 (*C*H_2 allylic), 18.2 (CH_3); diagnostic signals of the *cis*-anomer: ^{1}H NMR (500 MHz, Chloroform-*d,* HH-COSY, HSQC, HMBC, HH-NOESY): δ 3.78 (dd, *J* = 2.7, 1.0 Hz, 1H, H-2), 3.36 – 3.28 (m, 2H, H-1, H-5), 2.50 – 2.39 (m, 1H, C*H*H allylic); ^{13}C NMR (126 MHz, $CDCl_3$, HSQC): δ 134.9 (*C*H allyl), 117.3 (*C*H_2 allyl), 78.3 (C-1), 76.1 (C-5), 74.9 (C-2), 35.9 (*C*H_2 allylic), 19.6 (CH_3); HRMS: $[M+Na]^+$ calcd for $C_{30}H_{34}NaO_4$ 481.2349, found 481.2355.

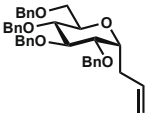


Allyl 2,3,4-tri-*O*-benzyl-1-deoxy-D-mannopyranoside (S12). The title compound was prepared according to general procedure I. Column chromatography (95:5 → 80:20, pentane:Et_2O) yielded the title compound (45 mg, 80 µmol, 80%, colorless oil, 1,2-*cis*:1,2-*trans*; 34:66). Spectroscopic data was in accordance with literature.[74] TLC: R_f 0.23 (1,2-*trans*) and 0.30 (1,2-*cis*) (pentane:Et_2O, 9:1, v:v); IR (thin film, cm^{-1}): 691, 1130, 1389, 1440, 1467, 2830, 2901; data of the *trans*-anomer: ^{1}H NMR (500 MHz, Chloroform-*d,* HH-COSY, HSQC, HMBC, HH-NOESY): δ 7.41 – 7.23 (m, 20H, CH_{arom}), 5.81 – 5.69 (m, 1H, C*H* allyl), 5.06 – 4.98 (m, 2H C*H*$_2$ allyl), 4.74 – 4.65 (m, 2H, C*H*H Bn, CH*H* Bn), 4.61 – 4.48 (m, 6H, C*H*H Bn, CH*H* Bn, C*H*H Bn, CH*H* Bn, C*H*H Bn, CH*H* Bn), 4.04 (ddd, *J* = 7.8, 6.1, 4.7 Hz, 1H, H-1), 3.88 – 3.81 (m, 2H, H-4, H-5), 3.80 – 3.74 (m, 2H, H-3, H-6), 3.71 (dd, *J* = 10.3, 3.5 Hz, 1H, H-6), 3.62 (dd, *J* = 4.9, 2.9 Hz, 1H, H-2), 2.39 – 2.27 (m, 2H, C*H*H allylic, CH*H* allylic); ^{13}C NMR (126 MHz, $CDCl_3$, HSQC): δ 138.6, 138.4, 138.4, 138.3 ($C_{q\text{-}arom}$), 134.0 (*C*H allyl), 128.5, 128.4, 128.4, 128.4, 128.3, 128.2, 128.2, 128.1, 128.1, 128.1, 128.0, 127.8, 127.7, 127.7, 127.6 (CH_{arom}), 117.3 (*C*H_2 allyl), 77.0 (C-3), 75.3 (C-2), 75.0, 74.0 (CH_2 Bn), 73.9 (C-5), 73.4 (CH_2 Bn), 72.5 (C-1), 72.2, 71.7 (CH_2 Bn), 69.3 (C-6), 33.9 (*C*H_2 allylic); diagnostic signals of the *cis*-anomer: ^{1}H NMR (500 MHz, Chloroform-*d,* HH-COSY, HSQC, HMBC, HH-NOESY): δ 4.87 (d, *J* = 10.8 Hz, 1H, C*H*H Bn), 4.78 (d, *J* = 11.7 Hz, 1H, C*H*H Bn), 3.46 (ddd, *J* = 9.7, 5.8, 1.8 Hz, 1H, H-5), 3.36 – 3.30 (m, 1H, H-1), 2.50 (dtt, *J* = 12.7, 6.4, 1.6 Hz, 1H, C*H*H allylic); ^{13}C NMR (126 MHz, $CDCl_3$, HSQC): δ 134.8 (*C*H allyl), 117.4 (*C*H_2 allyl), 80.0 (C-5), 78.4 (C-1), 75.4, 74.5, 73.6, 72.6 (CH_2 Bn), 69.9 (C-6). HRMS: $[M+Na]^+$ calcd for $C_{37}H_{40}NaO_5$ 587.2768, found 587.2781.

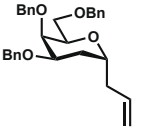


Allyl 2,3,4-tri-*O*-benzyl-1,2-dideoxy-D-mannopyranoside (S13). The title compound was prepared according to general procedure I. Column chromatography (95:5 → 80:20, pentane:Et_2O) yielded the title compound (42 mg, 92 µmol, 92%, colorless oil, 1,3-*cis*:1,3-*trans*; <2:98). TLC: R_f 0.14 (pentane:Et_2O, 9:1, v:v); $[\alpha]_D^{25}$ 48.6°; IR (thin film, cm^{-1}): 1113, 1397, 1433, 1456, 2890; ^{1}H NMR (500 MHz, Chloroform-*d,* HH-COSY, HSQC, HMBC, HH-NOESY): δ 7.37 – 7.23 (m, 15H, CH_{arom}), 5.82 – 5.70 (m, 1H, C*H* allyl), 5.08 –

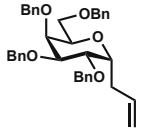
5.00 (m, 2H, C*H*$_2$ allyl), 4.78 (d, *J* = 11.1 Hz, 1H, C*H*H Bn), 4.63 – 4.47 (m, 5H, C*H*H Bn, CH*H* Bn, CH*H* Bn, C*H*H Bn, CH*H* Bn), 4.04 (tt, *J* = 7.4, 4.5 Hz, 1H, H-1), 3.83 – 3.73 (m, 3H, H-3, H-5, H-6), 3.70 – 3.63 (m, 1H, H-6), 3.54 (t, *J* = 7.1 Hz, 1H, H-4), 2.45 (dddt, *J* = 14.3, 7.9, 6.6, 1.4 Hz, 1H, C*H*H allylic), 2.22 (dtt, *J* = 14.3, 7.3, 1.2 Hz, 1H, CH*H* allylic), 1.99 (dt, *J* = 13.4, 4.3 Hz, 1H, H-2$_{eq}$), 1.76 (ddd, *J* = 13.3, 9.4, 5.0 Hz, 1H, H-2$_{ax}$); ^{13}C NMR (126 MHz, $CDCl_3$, HSQC): δ 138.6, 138.5, 138.4 ($C_{q\text{-}arom}$), 134.8 (*C*H allyl), 128.5, 128.5, 128.5, 128.1, 128.0, 127.8, 127.8, 127.8, 127.7 (CH_{arom}), 117.2 (*C*H$_2$ allyl), 77.0 (C-4), 76.5 (C-3), 74.2, 73.5 (CH$_2$ Bn), 72.9 (C-5), 71.5 (CH$_2$ Bn), 70.6 (C-1), 69.2 (C-6), 36.9 (*C*H$_2$ allylic), 32.5 (C-2); HRMS: [M+Na]$^+$ calcd for $C_{30}H_{34}NaO_4$ 481.2349, found 481.2350.



Allyl 2,3,4-tri-*O*-benzyl-1-deoxy-D-glucopyranoside (S14). The title compound was prepared according to general procedure I. Column chromatography (95:5 → 80:20, pentane:Et$_2$O) yielded the title compound (40 mg, 71 µmol, 71%, colorless oil, 1,2-*cis*:1,2-*trans*; >98:2). TLC: R$_f$ 0.23 (pentane:Et$_2$O, 9:1, v:v); $[\alpha]_D^{25}$ 28.7°; IR (thin film, cm^{-1}): 696, 1108, 1367, 1441, 2870; ^{1}H NMR (500 MHz, Chloroform-*d,* HH-COSY, HSQC, HMBC, HH-NOESY): δ 7.38 – 7.13 (m, 20H, CH_{arom}), 5.81 (dddd, *J* = 16.6, 10.2, 7.4, 6.3 Hz, 1H, C*H* allyl), 5.17 – 4.98 (m, 2H, C*H*$_2$ allyl), 4.93 (d, *J* = 11.0 Hz, 1H, C*H*H Bn), 4.84 – 4.76 (m, 2H, C*H*H Bn, CH*H* Bn), 4.69 (d, *J* = 11.6 Hz, 1H, C*H*H Bn), 4.67 – 4.58 (m, 2H, CH*H* Bn, C*H*H Bn), 4.50 – 4.44 (m, 2H, CH*H* Bn, CH*H* Bn), 4.13 (dt, *J* = 10.4, 5.0 Hz, 1H, H-1), 3.80 (dd, *J* = 9.5, 7.5 Hz, 1H, H-3), 3.76 (dd, *J* = 9.4, 5.5 Hz, 1H, H-2), 3.70 (dd, *J* = 10.6, 3.4 Hz, 1H, H-5), 3.67 – 3.59 (m, 3H, H-4, H-5, H-6), 2.56 – 2.44 (m, 2H, C*H*H allylic, CH*H* allylic); ^{13}C NMR (126 MHz, $CDCl_3$, HSQC): δ 138.9, 138.4, 138.3, 138.2 ($C_{q\text{-}arom}$), 134.9 (*C*H allyl), 128.6, 128.5, 128.5, 128.1, 128.1, 128.0, 128.0, 127.9, 127.9, 127.8, 127.8, 127.7 (CH_{arom}), 117.6 (*C*H$_2$ allyl), 82.6 (C-3), 79.8 (C-2), 78.2 (C-4), 75.6, 75.2 (CH$_2$ Bn), 73.8 (C-1), 73.6, 73.2 (CH$_2$ Bn), 71.2 (C-5), 69.0 (C-6), 29.9 (*C*H$_2$ allylic); HRMS: [M+Na]$^+$ calcd for $C_{37}H_{40}NaO_5$ 587.2768, found 587.2770.



Allyl 2,3,4-tri-*O*-benzyl-1,2-dideoxy-D-galactopyranoside (S15). The title compound was prepared according to general procedure I. Column chromatography (95:5 → 80:20, pentane:Et$_2$O) yielded the title compound (36 mg, 79 µmol, 79%, colorless oil, 1,3-*cis*:1,3-*trans*; <2:98). TLC: R$_f$ 0.218 (pentane:Et$_2$O, 9:1, v:v); $[\alpha]_D^{25}$ 17.7°; IR (thin film, cm^{-1}): 1089, 1389, 1447, 1458, 2867; ^{1}H NMR (500 MHz, Chloroform-*d,* HH-COSY, HSQC, HMBC, HH-NOESY): δ 7.47 – 7.20 (m, 15H, CH_{arom}), 5.77 (dddd, *J* = 17.0, 10.4, 7.5, 6.5 Hz, 1H, C*H* allyl), 5.12 – 4.97 (m, 2H, C*H*$_2$ allyl), 4.72 (d, *J* = 11.9 Hz, 1H, C*H*H Bn), 4.67 – 4.49 (m, 5H, CH*H* Bn, C*H*H Bn, CH*H* Bn, C*H*H Bn, CH*H* Bn,), 4.05 (dt, *J* = 7.9, 4.1 Hz, 1H, H-5), 3.99 (dt, *J* = 7.1, 3.6 Hz, 1H, H-1), 3.90 (dd, *J* = 10.6, 7.5 Hz, 1H, H-6), 3.81 (dt, *J* = 7.7, 3.2 Hz, 1H, H-3), 3.78 – 3.76 (m, 1H, H-4), 3.70 (dd, *J* = 10.6, 4.3 Hz, 1H, H-6), 2.36 (dddd, *J* = 13.9, 8.3, 6.8, 1.4 Hz, 1H, C*H*H allylic), 2.22 – 2.12 (m, 1H, CH*H* allylic), 2.06 (ddd, *J* = 13.3, 7.7, 4.1 Hz, 1H, H-2), 1.56 – 1.51 (m, 1H, H-2); ^{13}C NMR (126 MHz, $CDCl_3$, HSQC): δ 138.8, 138.7, 138.7 ($C_{q\text{-}arom}$), 135.0 (*C*H allyl), 128.5, 128.5, 128.4, 127.9, 127.7, 127.7, 127.6, 127.5, 127.4 (CH_{arom}), 117.1 (*C*H$_2$ allyl), 75.1 (C-4), 73.7 (C-3), 73.5 (C-5), 73.4, 72.6, 71.3 (CH$_2$ Bn), 68.0 (C-1), 68.0 (C-6), 38.0 (*C*H$_2$ allylic); HRMS: [M+Na]$^+$ calcd for $C_{30}H_{34}NaO_4$ 481.2349, found 481.2355.



Allyl 2,3,4-tri-*O*-benzyl-1-deoxy-D-galactopyranoside (S16). The title compound was prepared according to general procedure I. Column chromatography (95:5 → 80:20, pentane:Et$_2$O) yielded the title compound (56 mg, 80 µmol, 80%, colorless oil, 1,2-*cis*:1,2-*trans*; >98:2). TLC: R$_f$ 0.22 (pentane:Et$_2$O, 9:1, v:v); $[\alpha]_D^{25}$ 18.3°; IR (thin film, cm^{-1}): 680, 1160, 1370, 1441, 1459, 2879; 743; ^{1}H NMR (500 MHz,

Chloroform-*d*, HH-COSY, HSQC, HMBC, HH-NOESY): δ 7.91 – 6.50 (m, 20H, CH_{arom}), 5.75 (ddt, *J* = 17.1, 10.2, 6.9 Hz, 1H, C*H* allyl), 5.13 – 4.98 (m, 2H, CH_2 allyl), 4.80 – 4.63 (m, 2H, C*H*H Bn, C*H*H Bn), 4.65 – 4.39 (m, 6H, CH*H* Bn, CH*H* Bn, C*H*H Bn, CH*H* Bn, C*H*H Bn, CH*H* Bn,), 4.05 (bs, 1H, H-5), 4.03 – 3.97 (m, 1H, H-3), 4.00 (dd, *J* = 4.0, 2.6 Hz, 2H, H-1), 3.88 – 3.81 (m, 1H, H-6), 3.75 (s, 1H, H-4), 3.72 (dd, *J* = 6.9, 2.8 Hz, 1H, H-2), 3.66 (dd, *J* = 10.6, 4.7 Hz, 1H, H-6), 2.47 – 2.38 (m, 1H, C*H*H allylic), 2.38 – 2.29 (m, 1H, CH*H* allylic); ^{13}C NMR (126 MHz, $CDCl_3$, HSQC): δ 138.8, 138.7, 138.7, 138.5 ($C_{q\text{-}arom}$), 135.4 (*C*H allyl), 128.6, 128.6, 128.6, 128.5, 128.2, 128.1, 128.0, 128.0, 127.8, 127.8, 127.7 (CH_{arom}), 117.0 (CH_2 allyl), 76.7 (C-2), 76.7 (C-4), 74.5 (C-3), 73.4, 73.3, 73.3, 73.2 (CH_2 Bn), 73.0 (C-5), 70.8 (C-1), 67.5 (C-6), 33.9 (CH_2 allylic); HRMS: $[M+Na]^+$ calcd for $C_{37}H_{40}NaO_5$ 587.2768, found 587.2776.

References and notes

(1) Ayala, L.; Lucero, C. G.; Romero, J. A. C.; Tabacco, S. A.; Woerpel, K. A. Stereochemistry of Nucleophilic Substitution Reactions Depending upon Substituent: Evidence for Electrostatic Stabilization of Pseudoaxial Conformers of Oxocarbenium Ions by Heteroatom Substituents. *J. Am. Chem. Soc.* **2003**, *125* (50), 15521–15528.

(2) Walvoort, M. T. C.; Dinkelaar, J.; van den Bos, L. J.; Lodder, G.; Overkleeft, H. S.; Codée, J. D. C.; van der Marel, G. A. The Impact of Oxacarbenium Ion Conformers on the Stereochemical Outcome of Glycosylations. *Carbohydr. Res.* **2010**, *345* (10), 1252–1263.

(3) Crich, D. Mechanism of a Chemical Glycosylation Reaction. *Acc. Chem. Res.* **2010**, *43* (8), 1144–1153.

(4) Adero, P. O.; Amarasekara, H.; Wen, P.; Bohé, L.; Crich, D. The Experimental Evidence in Support of Glycosylation Mechanisms at the S_N1–S_N2 Interface. *Chem. Rev.* **2018**, *118* (17), 8242–8284.

(5) A. V. Demchenko. *Handbook of Chemical Glycosylation: Advances in Stereoselectivity and Therapeutic Relevance*; Wiley, **2008**.

(6) Bohé, L.; Crich, D. A Propos of Glycosyl Cations and the Mechanism of Chemical Glycosylation; the Current State of the Art. *Carbohydr. Res.* **2015**, *403*, 48–59.

(7) Bohé, L.; Crich, D. A Propos of Glycosyl Cations and the Mechanism of Chemical Glycosylation. *Comptes Rendus Chimie* **2011**, *14* (1), 3–16.

(8) Mydock, L. K.; Demchenko, A. V. Mechanism of Chemical *O*-Glycosylation: From Early Studies to Recent Discoveries. *Org. Biomol. Chem.* **2010**, *8* (3), 497–510.

(9) Nigudkar, S. S.; Demchenko, A. V. Stereocontrolled 1,2-*Cis* Glycosylation as the Driving Force of Progress in Synthetic Carbohydrate Chemistry. *Chem. Sci.* **2015**, *6* (5), 2687–2704.

(10) Hsu, C.-H.; Hung, S.-C.; Wu, C.-Y.; Wong, C.-H. Toward Automated Oligosaccharide Synthesis. *Angew. Chem. Int. Ed.* **2011**, *50* (50), 11872–11923.

(11) Lee, J.-C.; Greenberg, W. A.; Wong, C.-H. Programmable Reactivity-Based One-Pot Oligosaccharide Synthesis. *Nat. Protocols* **2007**, *1* (6), 3143–3152.

(12) Chen, J.; Hansen, T.; Zhang, Q.-J.; Liu, D.-Y.; Sun, Y.; Yan, H.; Codée, J. D. C.; Schmidt, R. R.; Sun, J.-S. 1-Picolinyl-5-Azido Thiosialosides: Versatile Donors for the Stereoselective Construction of Sialyl Linkages. *Angew. Chem. Int. Ed.* **2019**, *58* (47), 17000–17008.

(13) Hansen, T.; Ofman, T. P.; Vlaming, J. G. C.; Gagarinov, I. A.; Beek, J. van; Goté, T. A.; Tichem, J. M.; Ruijgrok, G.; Overkleeft, H. S.; Filippov, D. V.; van der Marel, G. A.; Codée, J. D. C. Reactivity-Stereoselectivity Mapping for the Assembly of Mycobacterium Marinum Lipooligosaccharides. *Angew. Chem. Int. Ed.* **2020**, *accepted*.

(14) Amyes, T. L.; Jencks, W. P. Lifetimes of Oxocarbenium Ions in Aqueous Solution from Common Ion Inhibition of the Solvolysis of .Alpha.-Azido Ethers by Added Azide Ion. *J. Am. Chem. Soc.* **1989**, *111* (20), 7888–7900.

(15) Chiappe, C.; Moro, G. L.; Munforte, P. Lifetime of the Glucosyl Oxocarbenium Ion and Stereoselectivity in the Glycosidation of Phenols with 1,2-Anhydro-3,4,6-Tri-*O*-Methyl-α-D-Glucopyranose. *Tetrahedron* **1997**, *53* (30), 10471–10478.

(16) Martin, A.; Arda, A.; Désiré, J.; Martin-Mingot, A.; Probst, N.; Sinaÿ, P.; Jiménez-Barbero, J.; Thibaudeau, S.; Blériot, Y. Catching Elusive Glycosyl Cations in a Condensed Phase with HF/SbF_5 Superacid. *Nat. Chem.* **2016**, *8* (2), 186–191.

(17) Elferink, H.; Severijnen, M. E.; Martens, J.; Mensink, R. A.; Berden, G.; Oomens, J.; Rutjes, F. P. J. T.; Rijs, A. M.; Boltje, T. J. Direct Experimental Characterization of Glycosyl Cations by Infrared Ion Spectroscopy. *J. Am. Chem. Soc.* **2018**, *140* (19), 6034–6038.

(18) Hansen, T.; Lebedel, L.; Remmerswaal, W. A.; van der Vorm, S.; Wander, D. P. A.; Somers, M.; Overkleeft, H. S.; Filippov, D. V.; Désiré, J.; Mingot, A.; Bleriot, Y.; van der Marel, G. A.; Thibaudeau, S.; Codée, J. D.

C. Defining the S_N1 Side of Glycosylation Reactions: Stereoselectivity of Glycopyranosyl Cations. *ACS Cent. Sci.* **2019**, *5* (5), 781–788.

(19) Hansen, T.; Elferink, H.; van Hengst, J. M. A.; Houthuijs, K. J.; Remmerswaal, W. A.; Kromm, A.; Berden, G.; van der Vorm, S.; Rijs, A. M.; Overkleeft, H. S.; Filippov, D. V.; Rutjes, F. P. J. T.; van der Marel, G. A.; Martens, J.; Oomens, J.; Codée, J. D. C.; Boltje, T. J. Characterization of Glycosyl Dioxolenium Ions and Their Role in Glycosylation Reactions. *Nat. Commun.* **2020**, *11* (1), 2664.

(20) Saito, K.; Ueoka, K.; Matsumoto, K.; Suga, S.; Nokami, T.; Yoshida, J. Indirect Cation-Flow Method: Flash Generation of Alkoxycarbenium Ions and Studies on the Stability of Glycosyl Cations. *Angew. Chem. Int. Ed.* **2011**, *50* (22), 5153–5156.

(21) Lebedel, L.; Ardá, A.; Martin, A.; Désiré, J.; Mingot, A.; Aufiero, M.; Aiguabella Font, N.; Gilmour, R.; Jiménez-Barbero, J.; Blériot, Y.; Thibaudeau, S. Structural and Computational Analysis of 2-Halogeno-Glycosyl Cations in the Presence of a Superacid: An Expansive Platform. *Angew. Chem. Int. Ed.* **2019**, *58* (39), 13758–13762.

(22) Elferink, H.; Mensink, R. A.; Castelijns, W. W. A.; Jansen, O.; Bruekers, J. P. J.; Martens, J.; Oomens, J.; Rijs, A. M.; Boltje, T. J. The Glycosylation Mechanisms of 6,3-Uronic Acid Lactones. *Angew. Chem. Int. Ed.* **2019**, *58* (26), 8746–8751.

(23) Marianski, M.; Mucha, E.; Greis, K.; Moon, S.; Pardo, A.; Kirschbaum, C.; Thomas, D. A.; Meijer, G.; Helden, G. von; Gilmore, K.; Seeberger, P. H.; Pagel, K. Remote Participation during Glycosylation Reactions of Galactose Building Blocks: Direct Evidence from Cryogenic Vibrational Spectroscopy. *Angew. Chem. Int. Ed.* **2020**, *59* (15), 6166–6171.

(24) Mucha, E.; Marianski, M.; Xu, F.-F.; Thomas, D. A.; Meijer, G.; von Helden, G.; Seeberger, P. H.; Pagel, K. Unravelling the Structure of Glycosyl Cations via Cold-Ion Infrared Spectroscopy. *Nature Communications* **2018**, *9* (1), 1–5.

(25) Hosoya, T.; Takano, T.; Kosma, P.; Rosenau, T. Theoretical Foundation for the Presence of Oxacarbenium Ions in Chemical Glycoside Synthesis. *J. Org. Chem.* **2014**, *79* (17), 7889–7894.

(26) Hosoya, T.; Kosma, P.; Rosenau, T. Contact Ion Pairs and Solvent-Separated Ion Pairs from D-Mannopyranosyl and D-Glucopyranosyl Triflates. *Carbohydr. Res.* **2015**, *401*, 127–131.

(27) Huang, M.; Garrett, G. E.; Birlirakis, N.; Bohé, L.; Pratt, D. A.; Crich, D. Dissecting the Mechanisms of a Class of Chemical Glycosylation Using Primary ^{13}C Kinetic Isotope Effects. *Nat. Chem.* **2012**, *4* (8), 663–667.

(28) Pierre Deslongchamps; Yves L. Dory; Shigui Li. R.U. Lemieux Award Lecture Hydrolysis of Acetals and Ketals. Position of Transition States along the Reaction Coordinates, and Stereoelectronic Effects. *Can. J. Chem.* **1994**, *10* (72), 2021–2027.

(29) Chamberland, S.; Ziller, J. W.; Woerpel, K. A. Structural Evidence That Alkoxy Substituents Adopt Electronically Preferred Pseudoaxial Orientations in Six-Membered Ring Dioxocarbenium Ions. *J. Am. Chem. Soc.* **2005**, *127* (15), 5322–5323.

(30) Romero, J. A. C.; Tabacco, S. A.; Woerpel, K. A. Stereochemical Reversal of Nucleophilic Substitution Reactions Depending upon Substituent: Reactions of Heteroatom-Substituted Six-Membered-Ring Oxocarbenium Ions through Pseudoaxial Conformers. *J. Am. Chem. Soc.* **2000**, *122* (1), 168–169.

(31) Vorm, S. van der; Hansen, T.; Overkleeft, H. S.; Marel, G. A. van der; Codée, J. D. C. The Influence of Acceptor Nucleophilicity on the Glycosylation Reaction Mechanism. *Chem. Sci.* **2017**, *8* (3), 1867–1875.

(32) Parent, J.-F.; Deslongchamps, G.; Deslongchamps, P. Bent Bond/Antiperiplanar Hypothesis: Modulating the Reactivity and the Selectivity in the Glycosylation of Bicyclic Pyranoside Models. *J. Org. Chem.* **2020**, *85* (6), 4220–4236.

(33) Crich, D.; Sharma, I. Is Donor–Acceptor Hydrogen Bonding Necessary for 4,6-*O*-Benzylidene-Directed β-Mannopyranosylation? Stereoselective Synthesis of β-*C*-Mannopyranosides and α-*C*-Glucopyranosides. *Org. Lett.* **2008**, *10* (21), 4731–4734.

(34) Seeman, J. I. The Curtin-Hammett Principle and the Winstein-Holness Equation: New Definition and Recent Extensions to Classical Concepts. *J. Chem. Educ.* **1986**, *63* (1), 42.

(35) Seeman, J. I. Effect of Conformational Change on Reactivity in Organic Chemistry. Evaluations, Applications, and Extensions of Curtin-Hammett Winstein-Holness Kinetics. *Chem. Rev.* **1983**, *83* (2), 83–134.

(36) van der Vorm, S.; Hansen, T.; van Rijssel, E. R.; Dekkers, R.; Madern, J. M.; Overkleeft, H. S.; Filippov, D. V.; van der Marel, G. A.; Codée, J. D. C. Furanosyl Oxocarbenium Ion Conformational Energy Landscape Maps as a Tool to Study the Glycosylation Stereoselectivity of 2-Azidofuranoses, 2-Fluorofuranoses and Methyl Furanosyl Uronates. *Chem. Eur. J.* **2019**, *25* (29), 7149–7157.

(37) van Rijssel, E. R.; van Delft, P.; Lodder, G.; Overkleeft, H. S.; Marel, G. A. van der; Filippov, D. V.; Codée, J. D. C. Furanosyl Oxocarbenium Ion Stability and Stereoselectivity. *Angew. Chem. Int. Ed.* **2014**, *53* (39), 10381–10385.

(38) Codée, J. D. C.; Litjens, R. E. J. N.; den Heeten, R.; Overkleeft, H. S.; van Boom, J. H.; van der Marel, G. A. Ph_2SO/Tf_2O: A Powerful Promotor System in Chemoselective Glycosylations Using Thioglycosides. *Org. Lett.* **2003**, *5* (9), 1519–1522.

(39) Becke, A. D. A New Mixing of Hartree–Fock and Local Density-functional Theories. *J. Chem. Phys.* **1993**, *98* (2), 1372–1377.

(40) Lee, C.; Yang, W.; Parr, R. G. Development of the Colle-Salvetti Correlation-Energy Formula into a Functional of the Electron Density. *Phys. Rev. B* **1988**, *37* (2), 785–789.

(41) Tomasi, J.; Mennucci, B.; Cammi, R. Quantum Mechanical Continuum Solvation Models. *Chem. Rev.* **2005**, *105* (8), 2999–3094.

(42) Peng, Q.; Duarte, F.; Paton, R. S. Computing Organic Stereoselectivity – from Concepts to Quantitative Calculations and Predictions. *Chem. Soc. Rev.* **2016**, *45* (22), 6093–6107.

(43) If $\Delta G^{\circ}{}^{3}{}_{H4} < \Delta G^{\circ}{}^{4}{}_{H3}$ then $\Delta\Delta G^{\ddagger}_{\text{addition}} = \Delta G^{\ddagger}_{\text{top}} - (\Delta G^{\ddagger}_{\text{bottom}} + \Delta\Delta G^{\circ})$, while if $\Delta G^{\circ}{}^{3}{}_{H4} > \Delta G^{\circ}{}^{4}{}_{H3}$ then $\Delta\Delta G^{\ddagger}_{\text{addition}} = (\Delta G^{\ddagger}_{\text{top}} + \Delta\Delta G^{\circ}) - \Delta G^{\ddagger}_{\text{bottom}}$ according to the work of the group Paton, see ref 33.

(44) Ammer, J.; Nolte, C.; Mayr, H. Free Energy Relationships for Reactions of Substituted Benzhydrylium Ions: From Enthalpy over Entropy to Diffusion Control. *J. Am. Chem. Soc.* **2012**, *134* (33), 13902–13911.

(45) Bickelhaupt, F. M.; Houk, K. N. Analyzing Reaction Rates with the Distortion/Interaction-Activation Strain Model. *Angew. Chem. Int. Ed.* **2018**, 10070–10086.

(46) Vermeeren, P.; van der Lubbe, S. C. C.; Fonseca Guerra, C.; Bickelhaupt, F. M.; Hamlin, T. A. Understanding Chemical Reactivity Using the Activation Strain Model. *Nat. Protocols* **2020**, *15* (2), 649–667.

(47) Zeist, W.-J. van; Bickelhaupt, F. M. The Activation Strain Model of Chemical Reactivity. *Org. Biomol. Chem.* **2010**, *8* (14), 3118–3127.

(48) Fernández, I.; Bickelhaupt, F. M. The Activation Strain Model and Molecular Orbital Theory: Understanding and Designing Chemical Reactions. *Chem. Soc. Rev.* **2014**, *43* (14), 4953–4967.

(49) Ess, D. H.; Houk, K. N. Distortion/Interaction Energy Control of 1,3-Dipolar Cycloaddition Reactivity. *J. Am. Chem. Soc.* **2007**, *129* (35), 10646–10647.

(50) Ess, D. H.; Houk, K. N. Theory of 1,3-Dipolar Cycloadditions: Distortion/Interaction and Frontier Molecular Orbital Models. *J. Am. Chem. Soc.* **2008**, *130* (31), 10187–10198.

(51) Galabov, B.; Koleva, G.; Schaefer III, H. F.; Allen, W. D. Nucleophilic Influences and Origin of the SN2 Allylic Effect. *Chem. Eur. J.* **2018**, *24* (45), 11637–11648.

(52) Vermeeren, P.; Hansen, T.; Jansen, P.; Swart, M.; Hamlin, T. A.; Bickelhaupt, F. M. A Unified Framework for Understanding Nucleophilicity and Protophilicity in the S_N2/E2 Competition. *Chem. Eur. J.* **2020**, *accepted*.

(53) Hansen, T.; Vermeeren, P.; Haim, A.; van Dorp, M. J. H.; Codée, J. D. C.; Bickelhaupt, F. M.; Hamlin, T. A. Regioselectivity of Epoxide Ring-Openings via S_N2 Reactions Under Basic and Acidic Conditions. *Eur. J. Org. Chem.* **2020**, *2020* (25), 3822–3828.

(54) Bickelhaupt, F. M.; Baerends, E. J. Kohn-Sham Density Functional Theory: Predicting and Understanding Chemistry. *Rev. Comp. Chem.* John Wiley & Sons, Ltd, **2007**; pp 1–86.

(55) Zhao, L.; Hopffgarten, M. von; Andrada, D. M.; Frenking, G. Energy Decomposition Analysis. *WIREs Comp. Mol. Sci.* **2018**, *8* (3).

(56) van Meer, R.; Gritsenko, O. V.; Baerends, E. J. Physical Meaning of Virtual Kohn–Sham Orbitals and Orbital Energies: An Ideal Basis for the Description of Molecular Excitations. *J. Chem. Theory Comput.* **2014**, *10* (10), 4432–4441.

(57) Gaussian 09, Revision D.01, M. J. Frisch, G. W. Trucks, H. B. Schlegel, G. E. Scuseria, M. A. Robb, J. R. Cheeseman, G. Scalmani, V. Barone, B. Mennucci, G. A. Petersson, H. Nakatsuji, M. Caricato, X. Li, H. P. Hratchian, A. F. Izmaylov, J. Bloino, G. Zheng, J. L. Sonnenberg, M. Hada, M. Ehara, K. Toyota, R. Fukuda, J. Hasegawa, M. Ishida, T. Nakajima, Y. Honda, O. Kitao, H. Nakai, T. Vreven, J. A. Montgomery, Jr., J. E. Peralta, F. Ogliaro, M. Bearpark, J. J. Heyd, E. Brothers, K. N. Kudin, V. N. Staroverov, T. Keith, R. Kobayashi, J. Normand, K. Raghavachari, A. Rendell, J. C. Burant, S. S. Iyengar, J. Tomasi, M. Cossi, N. Rega, J. M. Millam, M. Klene, J. E. Knox, J. B. Cross, V. Bakken, C. Adamo, J. Jaramillo, R. Gomperts, R. E. Stratmann, O. Yazyev, A. J. Austin, R. Cammi, C. Pomelli, J. W. Ochterski, R. L. Martin, K. Morokuma, V. G. Zakrzewski, G. A. Voth, P. Salvador, J. J. Dannenberg, S. Dapprich, A. D. Daniels, O. Farkas, J. B. Foresman, J. V. Ortiz, J. Cioslowski, and D. J. Fox, Gaussian, Inc., Wallingford CT, **2013**.

(58) Bootsma, A. N.; Wheeler, S. Popular Integration Grids Can Result in Large Errors in DFT-Computed Free Energies. **2019**..

(59) Sun, X.; Soini, T. M.; Poater, J.; Hamlin, T. A.; Bickelhaupt, F. M. PyFrag 2019—Automating the Exploration and Analysis of Reaction Mechanisms. *J. Comp. Chem.* **2019**, *40* (25), 2227–2233.

(60) Legault, C.Y.; CYLview, 1.0b, Université de Sherbrooke, **2009** (cylview.org).

(61) Ribeiro, R. F.; Marenich, A. V.; Cramer, C. J.; Truhlar, D. G. Use of Solution-Phase Vibrational Frequencies in Continuum Models for the Free Energy of Solvation. *J. Phys. Chem. B* **2011**, *115* (49), 14556–14562.

(62) ADF2017, SCM, Theoretical Chemistry, Vrije Universiteit, Amsterdam (The Netherlands), **2017**.

(63) Velde, G. te; Bickelhaupt, F. M.; Baerends, E. J.; Guerra, C. F.; Gisbergen, S. J. A. van; Snijders, J. G.; Ziegler, T. Chemistry with ADF. *J. Comp. Chem.* **2001**, *22* (9), 931–967.

(64) Fonseca Guerra, C.; Snijders, J. G.; te Velde, G.; Baerends, E. J. Towards an Order-*N* DFT Method. *Theor Chem Acc* **1998**, *99* (6), 391–403.
(65) Van Lenthe, E.; Baerends, E. J. Optimized Slater-Type Basis Sets for the Elements 1-118. *J Comput Chem* **2003**, *24* (9), 1142–1156.
(66) Franchini, M.; Philipsen, P. H. T.; Visscher, L. The Becke Fuzzy Cells Integration Scheme in the Amsterdam Density Functional Program Suite. *J. Comp. Chem.* **2013**, *34* (21), 1819–1827.
(67) Franchini, M.; Philipsen, P. H. T.; van Lenthe, E.; Visscher, L. Accurate Coulomb Potentials for Periodic and Molecular Systems through Density Fitting. *J. Chem. Theory Comput.* **2014**, *10* (5), 1994–2004.
(68) van Lenthe, E.; Baerends, E. J.; Snijders, J. G. Construction of the Foldy–Wouthuysen Transformation and Solution of the Dirac Equation Using Large Components Only. *J. Chem. Phys.* **1996**, *105* (6), 2373–2377.
(69) van Lenthe, E.; Baerends, E. J.; Snijders, J. G. Relativistic Total Energy Using Regular Approximations. *J. Chem. Phys.* **1994**, *101* (11), 9783–9792.
(70) Hamlin, T. A.; van Beek, B.; Wolters, L. P.; Bickelhaupt, F. M. Nucleophilic Substitution in Solution: Activation Strain Analysis of Weak and Strong Solvent Effects. *Chem. Eur. J.* **2018**, *24* (22), 5927–5938.
(71) Beek, B. van; Bochove, M. A. van; Hamlin, T. A.; Bickelhaupt, F. M. Nucleophilic Substitution at Di- and Triphosphates: Leaving Group Ability of Phosphate versus Diphosphate. *Electron. Struct.* **2019**, *1* (2).
(72) Lucero, C. G.; Woerpel, K. A. Stereoselective *C*-Glycosylation Reactions of Pyranoses: The Conformational Preference and Reactions of the Mannosyl Cation. *J. Org. Chem.* **2006**, *71* (7), 2641–2647.
(73) Uchiyama, T.; Woltering, T. J.; Wong, W.; Lin, C.-C.; Kajimoto, T.; Takebayashi, M.; Wéitz-Schmidt, G.; Asakura, T.; Noda, M.; Wong, C.-H. Design and Synthesis of *C*-Linked Fucosides as Inhibitors of E-Selectin. *Bio. Med. Chem.* **1996**, *4* (7), 1149–1165.
(74) Bertozzi, C.; Bednarski, M. *C*-Glycosyl Compounds Bind to Receptors on the Surface of Escherichia Coli and Can Target Proteins to the Organism. *Carbohydr. Res.* **1992**, *223*, 243–253.